

A Hubble & Spitzer Space Telescope Survey for Gravitationally-Lensed Galaxies: Further Evidence for a Significant Population of Low Luminosity Galaxies beyond Redshift Seven

Johan Richard ¹, Daniel P. Stark¹, Richard S. Ellis¹, Matthew R. George^{1,3}, Eiichi Egami⁴,
Jean-Paul Kneib ^{1,2}, Graham P. Smith ^{1,5}

ABSTRACT

We present the results of a systematic search for gravitationally-lensed continuum Lyman break ‘drop-outs’ beyond a redshift 7 conducted via very deep imaging through six foreground clusters undertaken with the Hubble and Spitzer Space Telescopes. The survey has yielded 10 z -band and 2 J -band drop-out candidates to photometric limits of $J_{110} \simeq 26.2$ AB (5σ). Taking into account the magnifications afforded by our clusters (1-4 magnitudes), we probe the presence of $z > 7$ sources to unlensed limits of $J_{110} \simeq 30$ AB, fainter than those charted in the Hubble Ultradeep Field. To verify the fidelity of our candidates we conduct a number of tests for instrumental effects which would lead to spurious detections, and carefully evaluate the likelihood of foreground contamination by considering photometric uncertainties in the drop-out signature, the upper limits from stacked IRAC data and the statistics of multiply-imaged sources. Overall, we conclude that we can expect at least 60% of our sample of z -band drop-outs are likely to be at high redshift. An ambitious infrared spectroscopic campaign undertaken with the NIRSPEC spectrograph at the WM Keck Observatory for seven of the most promising candidates failed to detect any Lyman α emission highlighting the challenge of making further progress in this field. While the volume density of high redshift sources will likely remain uncertain until more

¹Department of Astrophysics, California Institute of Technology, MS 105-24, Pasadena, CA 91125; johan@astro.caltech.edu

²Observatoire Astronomique de Marseille-Provence, Traverse du Siphon - BP 8, 13376 Marseille Cedex 12, France

³Current address: Institute of Astronomy, Madingley Road, Cambridge, CB3 0HA, UK

⁴Steward Observatory, University of Arizona, 933 N. Cherry Avenue, Tucson, AZ 85721

⁵School of Physics and Astronomy, University of Birmingham, Edgbaston, Birmingham B15 2TT, UK

powerful facilities are available, our data provides the first potentially interesting constraints on the UV luminosity function at $z \simeq 7.5$ at intrinsically faint limits. We discuss the implications of our results in the context of the hypothesis that the bulk of the reionizing photons in the era $7 < z < 12$ arise in low luminosity galaxies undetected by conventional surveys.

Subject headings: cosmology: observations — galaxies: evolution — galaxies: formation — galaxies: high-redshift — gravitational lensing

1. Introduction

Very little is currently known about the abundance and luminosity distribution of star-forming sources beyond $z \gtrsim 7$. The two principal techniques used to locate distant star forming sources at lower redshifts, the Lyman-break ‘drop-out’ technique (Bouwens et al. 2006) and the location of Lyman α emitters (Kashikawa et al. 2006; Shimasaku et al. 2006), become challenged by the lower performance of infrared instruments. In addition, the likely sources are much fainter, particularly if an increasing fraction are sub-luminous as might be expected given mass assembly is at an early stage (Loeb & Barkana 2001; Choudhury & Ferrara 2007). Despite these hurdles, it seems reasonable to expect that there is an abundance of star-forming galaxies at these epochs. The improved measurement of the optical depth to electron scattering derived from temperature-polarization correlations in the microwave background (Komatsu et al. 2008) suggests reionization occurred around $z_{reion} = 10.8 \pm 1.4$ assuming it happened instantaneously; more probably it proceeded over an extended redshift window $7 < z < 12$ (Spergel et al. 2007). Moreover, the detection of galaxies at $z \sim 6$ with significant stellar masses and mature stellar populations (Stark et al. 2007a; Eyles et al. 2007) and the ubiquity of ionized carbon in the intergalactic medium probed by the highest redshift QSOs (Songaila 2004; Ryan-Weber et al. 2006), together demand a significant amount of star-formation at earlier times, possibly enough to cause reionization. Although uncertainties remain, these independent arguments strongly motivate the search for $z > 7$ star-forming sources.

Most of the early progress in this quest has been made through the publicly-available deep Hubble Space Telescope (HST) images. The Great Observatories Origins Deep Survey (GOODS, Dickinson et al. (2003)), the Hubble Ultra Deep Field (Beckwith et al. 2006, UDF) and its associated parallel fields have been used to search for ‘drop-outs’ in the i_{775} (Bouwens et al. 2006; Bunker et al. 2004), z_{850} (Bouwens & Illingworth 2006; Bouwens et al. 2008) and J_{110} (Bouwens et al. 2005, 2008) bands, corresponding to effective source redshifts of $z \simeq 6, 7.5$ and 10. These studies found a highly uncertain number density of candidates,

none of which has been confirmed spectroscopically at $z > 7$. However, taken at face value, the overall conclusion from these ultradeep images is that the declining abundance of luminous star forming sources beyond $z \simeq 7$ is insufficient to account for reionization. Although there is no guarantee that star-forming sources did reionize the Universe at $z \simeq 10$, a possible solution is that the bulk of the early star formation resides in an undetected population of intrinsically sub-luminous sources (Stark et al. 2007a).

Prior to the availability of the next generation of telescopes, gravitational lensing is an effective means to evaluate this hypothesis. Depending on the method, foreground massive clusters can provide a magnification boost of $\times 5 - 30$ in flux (for unresolved sources) or in size (for resolved sources). An analysis by Stark et al. (2007c) concluded that lensing surveys should be able to find ample candidates at $z \gtrsim 7$, permitting follow-up spectroscopy and detailed studies at sensitivity limits that would be unachievable otherwise.

A first attempt at constraining the abundance of lensed drop-out galaxies at $6 \lesssim z \lesssim 10$ was made by Richard et al. (2006) using deep ISAAC near-infrared images obtained at the ESO VLT. A number of faint (intrinsic $H(AB) \sim 26$) candidates were identified in two clusters, where the *magnification factor* μ ranged from 0.4 to 2.5 magnitudes. This analysis suggested a star formation rate density at $z \simeq 7.5 \sim \times 10$ higher than that derived by Bouwens et al. (2004). Deeper NICMOS images have failed to confirm some of these sources (Richard et al., in preparation) and both incompleteness and possible contamination from lower redshift sources have served to illustrate the difficulties in making progress beyond $z \simeq 7$ using ground-based facilities.

In a parallel effort, Stark et al. (2007b) concentrated on the much smaller regions of very high magnification ($\mu > 3$ mags) termed the ‘critical lines’ of the lensing clusters. Using NIRSPEC on the Keck telescope they undertook a ‘blind’ spectroscopic search for lensed Lyman- α emitters in the redshift range $8.5 < z < 10.4$. Despite the very small volumes probed in this unique survey, 6 faint candidates emerged across 9 clusters. Exhaustive follow-up imaging and spectroscopy appears to support the Ly α interpretation for these single emission line features. Taking into account the uncertainties, Stark et al. 2007b concluded that the abundance of low-luminosity emitters in this redshift window may exceed 0.2 Mpc^{-3} , suggestive of a major contribution of low luminosity star-forming galaxies to cosmic reionization.

The caveats concerning this conclusion were discussed in detail by Stark et al. Although representing a unique search for early star-forming sources at limits well beyond those probed otherwise, the volumes addressed are modest and significantly affected by cosmic variance. The 6 candidates were found in only 3 of the 9 lensing clusters; 6 clusters had no convincing candidates. Although Stark et al. were unable to prove, unambiguously, that the detected

emission is due to Lyman α , the null detection of associated lines was used as an argument for rejecting lower redshift emission for most of their candidates.. Their conclusion that the bulk of the reionizing photons arose from low luminosity ($\simeq 0.1 M_{\odot} \text{ yr}^{-1}$) star-forming sources can be verified by this independent search for lensed *continuum* drop-outs at $z > 7$.

In searching for faint lensed drop-outs, the advantage of HST over a ground-based survey such as that undertaken by Richard et al. (2006) is considerable. The ACS and NICMOS cameras are much more sensitive, not only because of the reduced space background, but also because the typical sources have angular sizes of $0.2''$ or less (Ellis et al. 2001). With similar exposure times, NICMOS can readily attain a depth of 26.5 AB mag, ~ 1 magnitude deeper than the earlier VLT/ISAAC project. Viewed through a typical $z \sim 0.2$ cluster, the NICMOS field (0.8×0.8 arcmin) closely matches the area of moderate to high magnification factors ($\mu \sim 1 - 4$ mag). The increased depth of HST imaging, combined with the lensing magnification, assures the detection of sources even fainter than those located in the UDF (Bouwens et al. 2008).

Early studies of lensed drop-outs with HST have served to illustrate the potential. Kneib et al. (2004) located a source at $z \simeq 6.8$ behind the cluster Abell 2218. This source forms a triply-imaged system with two bright elongated arcs, easily recognized as morphologically-similar in ACS and NICMOS images. Follow-up observations with Spitzer (Egami et al. 2005) provided improved constraints on the photometric redshift, stellar mass ($M \sim 10^9 M_{\odot}$) and past star formation history. Very recently, a similar $z \simeq 7.6$ lensed source was found by Bradley et al. (2008) but this was not multiply-imaged. A semi-analytic analysis, empirically calibrated using the luminosity functions of Lyman- α emitters and drop-out galaxies at $z \sim 5 - 6$ (Stark et al. 2007c) predicts that such a NICMOS/ACS lensed imaging survey should typically detect 0.5-1 sources per cluster in the redshift range $7.0 < z < 8.5$.

The present program represents the logical next step: a concerted effort to verify the hypothesis advocated by Stark et al. as well as its associated predictions via deep imaging of 6 lensing clusters with HST (GO 10504: PI: Ellis) and Spitzer (GO-20439, PI: E.Egami). The primary goal is to determine the abundance of intrinsically sub-luminous z and J_{110} drop-outs, and to derive independent constraints on the possible contribution of low luminosity sources to cosmic reionization.

The paper is organized as follows. In §2 we present the new HST/Spitzer and associated ground-based imaging observations and their data reduction. A discussion of the means of selecting the drop-out candidates is presented alongside a catalog in §3. Issues of completeness and contamination by spurious and foreground sources are discussed. We conclude that a significant fraction of our candidates are likely to be at high redshift. We then describe a Keck spectroscopic follow-up campaign in §4 which attempts to detect Lyman α emission

from some of the most promising candidates. In §5 we discuss the UV luminosity function at $z \simeq 7.5$ and review the implications in the context of the possible contribution of low luminosity to cosmic reionization. Our conclusions are summarized in §6.

All magnitudes given in this paper are standardized within the AB magnitude system (Oke 1974). We assume a flat universe and $(\Omega_m, \Omega_\Lambda, h) = (0.3, 0.7, 0.7)$ whenever necessary.

2. Survey Strategy, Observations and Data Reduction

We begin by discussing the selection of lensing clusters, the imaging datasets we have secured to select the various drop-out candidates and validate their high redshift nature, and the image processing steps taken to produce photometric catalogs. In addition to the HST and Spitzer datasets which form the fulcrum of this study, we have added ground-based imaging in both the optical and K band. In general terms, the HST data acts as the primary source of drop-out candidates and the associated data is used to constrain the likely redshift distribution.

2.1. Lensing Cluster Sample

Our primary criterion in selecting foreground clusters for this lensing survey is the value of the magnification factor expected for sources beyond $z \simeq 7$ and the uncertainty implied in this estimate based on an understanding of the mass model. We considered a number of massive clusters at $z \simeq 0.1 - 0.5$ with well-understood mass models capable of producing regions of strong magnification which match the imaging area of the HST cameras. Even though the area enclosed by the critical line for a $z \simeq 7$ source is sufficient for the design of the program, a precise mass model is a clear advantage in determining the magnification of a particular source, as well as for predicting accurately the location of any multiple images.

Our strategy parallels that discussed in some detail by Stark et al. Indeed that Lyman α critical line survey placed greater demands on the reliability of the cluster mass models as the magnifications are more extreme and positional uncertainties in the image plane are critical. Notwithstanding this challenge, Stark et al. found that the typical magnification uncertainties for their candidates were only $\simeq 30\%$ and that errors in the critical line location were usually only ± 1 arcsec or so.

In the present survey, six clusters was considered the minimum number necessary to mitigate the effects of cosmic variance (Stark et al. 2007c) while being consistent with the observing time available. In considering the final tally of clusters, we included clusters which

we have modeled with the latest version of the Lenstool¹ software (Jullo et al. 2007). This improved code provides a new Bayesian optimization method to derive error estimates for each optimized parameter. Following the discussion in Richard et al. (2007) and Limousin et al. (2007), this optimization can be used to compute error estimates on the individual magnification factors for each of our sources.

Wherever possible, we included clusters with usefully deep archival HST and Spitzer/IRAC data. Deep optical ($AB > 27.0$) ACS and/or WFPC2 images, previously used for the identification of multiple images during the development of the mass models, reduce the probability of low redshift contaminants. IRAC images at 3.6 and 4.5 μm , to the same 1 μJy sensitivity as our previous work in Abell 2218 Egami et al. (2005), are available as part of a Spitzer Lensing Cluster Survey (GTO 83, PI: G. Rieke) or publicly from the archive (GTO 64, PI: G. Fazio). Finally, we required that each of the selected clusters be visible from the northern hemisphere, in order to facilitate spectroscopic follow-up and further K -band imaging with the Keck and Subaru telescopes.

The six clusters satisfying the above criteria are presented in Table 1. Although the references cite the most recently-published mass models, as described above, in each case we have utilized the available multiple images and their redshifts in improving these mass models using Lenstool. Four out of the six clusters are in common with the sample adopted by Stark et al.

2.2. Hubble Space Telescope Data and Reduction

Our large program with HST (GO 10504, PI: Ellis) comprised deep observations in the z_{850} , J_{100} and H_{160} bands, using the Wide Field Camera of ACS and the NIC3 configuration of NICMOS. The region enclosed by the critical line for the wanted $z > 7$ sources was typically covered by two NICMOS pointings per cluster, usually adjacent. This ensured a magnification gain of $\mu \sim 1$ to 4 magnitudes, with a typical value $\mu \sim 2$ mags, throughout the NICMOS imaged field (Fig. 1).

The ACS images were reduced with the `multidrizzle` software (Koekemoer et al. 2002). This removes cosmic rays and bad pixels and combines the dithered frames to correct for camera distortion. The output pixel scale was fixed at 0.04'' and we used a `pixfrac` value of 0.8 for reducing the area of the input pixels. We made small corrections to the absolute astrometry to allow for ACS frames taken at different epochs (e.g. Abell 2218 in the F850LP

¹Publically available, see <http://www.oamp.fr/cosmology/lenstool> to download the latest version

band, see Table 2). These corrections were computed by correlating the catalog positions of bright objects detected in the overlapping regions.

Each single set of NICMOS observations consists of 8 (in F110W) and 10 (F160W) frames of ~ 1000 secs, taken with the NIC3 camera using the SPARS64 or SPARS128 sampling sequences. A basic reduction was performed by adopting the procedures given in the NICMOS data reduction handbook². Starting with the post-calibrated frames, bad pixels are flagged and rejected based on individual histograms, cosmic ray are rejected using the LACOSMIC (van Dokkum 2001) IRAF procedures, frame-to-frame shifts are measured using a cross correlation technique, and all frames are drizzled onto a NICMOS pixel scale ($0.2''$) to produce an initial reduced image. This then serves as a comparison for each individual frame so that deviant pixels can be flagged to improve image quality in a second drizzling operation, this time undertaken with an image pixel of $0.1''$, to obtain a better sampling.

These initial images reveal a number of cosmetic effects (bias and flat residuals, bad columns and bad pixels, quadrant-to-quadrant variations, background variations) that led to a second stage of image reduction. We used an improved pixel mask to flag several bad columns and bad pixels close to the frame edges, and we examined each frame individually in order to remove bias and flat residuals and quadrant-to-quadrant variations. Finally, we subtracted a smoothed background obtained by averaging the frames of all the observed clusters, masking every pixel lying on a physical object. In order to combine all NICMOS observations of a given cluster, usually taken at different epochs and with slight variations in the sky orientation, the individually-reduced images were registered onto the wider field ACS data prior to the final drizzling procedure and combination into a NICMOS mosaiced image.

The NICMOS data acts as the primary basis for selecting our drop-out candidates in association with non-detections in very deep optical data. In addition to our own ACS data, we reduced deep ACS and WFPC2 images from the archive for each cluster in our sample (Table 2). As with the ACS F850LP data undertaken in our own program, we reduced these data using the IRAF procedures `multidrizzle` and `drizzle` as discussed above.

2.3. Ground-based Data and Reduction

As mentioned, optical non-detection to deep limits is a key necessity in considering the validity of our drop-out candidates. Most clusters have complete optical coverage with HST

²<http://www.stsci.edu/hst/nicmos/documents/handbooks/handbooks/DataHandbookv7/>

(from ~ 400 to $\sim 850\text{nm}$) useful for this purpose. However, Abell 2219 has F702W only, and Abell 2390 has F555W and F814W only. For these two clusters, additional very deep ground-based images taken with the CFH12k camera on CFHT (Bardeau et al. 2007) were also examined (Table 4).

Ground-based photometry in the K band can likewise provide additional information for z drop-outs, improving the photometric redshift estimates, and for the reliability of J drop-outs where otherwise only a single color would be available (see Section 3.1). Although a challenging undertaking given the depth of the ACS and NICMOS data, we conducted various K -band imaging observations of clusters using the Keck and Subaru telescopes.

The Near Infrared Camera (NIRC) on Keck-I was used on July 2006 to observe the central regions of the clusters Abell 2218 and Abell 2219. The square field of NIRC ($38''$ a side) is slightly smaller than that of NICMOS therefore we concentrated these observations on our best z and J -band drop-outs in each cluster (see section 3.1). The seeing was stable and in the range $0.5\text{--}0.6''$. We used dithered exposures of $6 \text{ coadds} \times 10 \text{ secs}$ exposure time each. The NIRC pointing in Abell 2218 was partially covered, in the region of one of the drop-outs, by previous NIRC observations obtained in 22/23 July 2002 (A. Blain & N. Reddy 2003, private communication).

The Multi-Object InfraRed Camera and Spectrograph (MOIRCS) (Ichikawa et al. 2006) at Subaru was also used during two observing campaigns, in August 2006 and May 2007. The larger field of view ($7' \times 4'$) of this camera ensures a complete coverage of the NICMOS, ACS and IRAC data in each cluster. The four clusters in common with the Stark et al. sample (Abell 2218, 2219, 2390 and CL0024) were imaged for ~ 5 hours each under very good seeing conditions ($0.3\text{--}0.4''$) using dithered exposures of 50 secs duration. We used the MCSRED software package³ to perform the flat-fielding, sky-subtraction, distortion correction and mosaicing of individual images. The MCSRED package also includes MOIRCS-specific tasks which correct for quadrant shifts and to fit sky residuals. The depth reached by the MOIRCS imaging data ($K_{AB} \sim 26.1$) in Abell 2218 and Abell 2219 is similar or deeper than the NIRC observations of the same fields. Therefore, we used the NIRC images as independent check for the MOIRCS photometric measurements, performed under better seeing conditions.

³available from <http://www.naoj.org/staff/ichi/MCSRED/mcsred.html>

2.4. Spitzer Data and Reduction

Each cluster has been observed at 3.6, 4.5, 5.8, and 8.0 μm using the Infrared Array Camera (IRAC; Fazio et al. (2004)) on board the *Spitzer* Space Telescope (Werner et al. 2004). In this paper, we only discuss the first two channels (3.6 and 4.5 μm) where the depth achieved is potentially useful in comparison with our ACS and NICMOS data. Each of the IRAC channels uses a separate detector array, and the 3.6 μm channel ($\lambda_c = 3.56\mu\text{m}$; $\Delta\lambda = 0.75\mu\text{m}$) and 4.5 μm channel ($\lambda_c = 4.52\mu\text{m}$; $\Delta\lambda = 1.01\mu\text{m}$) use 256×256 InSb arrays with a pixel scale of $1''.2 \text{ pixel}^{-1}$, producing a field of view of $5''.2 \times 5''.2$. A frame time of 200 seconds was used with the small-step cycling dither pattern initially, but this was later changed to 100 seconds with the medium-step cycling pattern for a better removal of cosmic rays and other artifacts.

Most of the IRAC data come from the Spitzer GTO program PID:83 (PI: G. Rieke). The total integration time is 2400 s per channel, usually obtained at two different epochs. CL0024 was observed as part of another GTO program PID:64 (PI: G. Fazio) with the integration times of 2400 s at 3.6 μm and 3600 s at 4.5 μm . Abell 2218 was the subject of a deeper GO campaign (PID:20439, PI: Egami), and was observed for ~ 10 hours per channel, split into 6 separate observations (AORs). When these GO data are combined with those of the GTO program (PID:83), the resultant total integration time is 37700 seconds per channel. The corresponding depth (25.5 AB) in this particular cluster is much closer to the magnitude of our high redshift candidates. (see Table2 for a summary of the data).

In producing the IRAC images, we started with the basic calibrated data (BCD) of each individual frame produced by the SSC pipeline, and combined them using a custom IDL mosaicing routine as presented in Egami et al. (2005). The final pixel size of the IRAC mosaics is $0.6''/\text{pixel}$, half that of the original data. A conservative estimate for the absolute calibration uncertainty is 10%.

2.5. Foreground Subtraction

Although the magnification afforded by lensing clusters offers a unique gain in probing the distant universe, the central regions are dominated by bright, extended spheroidal galaxies which obstruct and whose light increases the background level. Fortunately their morphology is usually regular and their light distribution can be accurately modeled by a sequence of elliptical isophotes. Since the major contributor to this deficiency is the brightest cluster galaxy (BCG), we have modeled and subtracted its light for each cluster in the ACS (I_{850} band) and NICMOS images using the IRAF task `ellipse`. Apart from a small region

($\sim 1.0''$ radius) around the core of the removed BCG, this frees the image from the majority of the contamination in highly magnified regions close to the critical line, and aids in the detection of underlying sources (see Figure 2).

Foreground subtraction is more challenging for the IRAC images because of the much coarser PSF. The smaller number of available pixels per galaxy prevents the use of the `ellipse` modeling technique discussed above. Instead we adopted the `ellipse` model of the BCG derived from the NICMOS data and, on the assumption that the spectral energy distribution is identical across the galaxy at these long wavelengths, convolved this model with the IRAC PSF derived by stacking ~ 50 bright isolated point sources. This model of the BCG was subtracted after an appropriate scaling factor. We found this procedure to be very effective, with residuals from the subtraction confined within a $2.0''$ radius region (Figure 2).

2.6. Final Photometry

The primary filters we will use for identifying the near-infrared drop-outs are the ACS z_{850} and NICMOS J_{110} , H_{160} bands available for each cluster. The bulk of the rest-frame UV flux is contained in the two reddest filters at high redshift, so we require all sources to be detected in both. The signal to noise ratio is improved by combining the J and H images, once normalized to a similar noise level, to form a single $< J + H >$ detection image. This provides a more accurate measurement of the centroid and geometrical parameters of these objects,

We use the “double-image” mode of the SExtractor package Bertin & Arnouts (1996) to detect objects and compute magnitudes within a $0.6''$ -diameter aperture. The corresponding aperture corrections, of 0.3 and 0.6 magnitudes for ACS and NICMOS respectively, were estimated using bright isolated unsaturated stars.

The drizzling procedure used in the HST reductions, while conserving flux, does introduce correlations between neighboring pixels and hence false error estimates (Casertano 2000). We applied their equation [A20] to the SExtractor photometric errors. Dithered exposures also introduce a varying effective exposure time across the mosaic, this effect is clearly apparent close to the boundaries of the field. We constructed a corresponding weight map, proportional to the effective integration time at each pixel position in the detection image, and used it as an input parameter of SExtractor. This ensures source detection at a uniform noise level across each image.

The background noise level σ was measured for the ACS and NICMOS images in order to estimate the achievable photometric limits in each band. The 5σ values, measured in 0.3 and 0.6''-diameter apertures for ACS and NICMOS respectively, are reported in Table 2 after including the aperture corrections. The NICMOS limits (typically 26.2 and 26.5 AB in J and H respectively) are about 1.0 to 1.5 magnitudes brighter than the UDF (Bouwens et al. 2004), but this shortfall is counterbalanced by the magnification (between 1 and 4 magnitudes).

We computed the completeness limits in each NICMOS filter used for source detection by adding artificial unresolved sources in the magnitude range 23-28 AB. Such sources were added 1000 times at 30 different random locations on the image and then extracted using the same photometric techniques as used for the real sources. Only blank regions were chosen for this exercise, defined after application of a 5σ threshold to mask pixels lying on top of bright objects. The 50% completeness values derived in this way are listed for each cluster and band in Table 2. Typically, our NICMOS data is 50% complete to $J_{110} \simeq 25.9$ AB and to $H_{160} \simeq 26.05$ AB. For each eventual drop-out candidate (§3.3), we will assign a completeness factor, S_{comp} , based on its magnitude, that will be taken into account in estimating the high redshift luminosity function.

3. High Redshift Candidates

We now turn to the selection of our high redshift candidates. The primary selection will be based upon the $z_{850} - J_{110}$ color for the z drop-outs at redshifts $z \simeq 7-8$, and the $J_{110} - H_{160}$ color for the J -band drop-outs at redshifts $z \simeq 8-10$. This section has two components. First we discuss the optimum color criteria for drop-out selection, the degree of completeness and issues of possible contamination from spurious artefacts at these faint limits. In this way we establish a robust set of candidates whose likelihood of being at high redshift we then assess in the second part of this section using additional criteria including their photometry at other wavelengths and location with respect to the cluster mass model. The catalog of candidates is summarized in §3.3.

3.1. Photometric Selection and Completeness

The primary concern in selecting high redshift drop-outs from photometric data alone is the issue of contamination from lower redshift objects, including $z \simeq 2$ early-type galaxies, dust-reddened objects over a wide redshift range or low mass Galactic stars with deep molec-

ular absorption bands. Figure 3 illustrates the problem. A single color-cut fails to isolate z -band drop-outs from a variety of $z \simeq 2-4$ sources and the confusion is worse for J -band drop-outs.

This problem has formed the basis of much discussion in the literature. For the z -band drop-outs, contamination can be reduced by considering a second color (Stanway et al. 2004), of which the most useful with NICMOS data is $J_{110} - H_{160}$ (Bouwens et al. 2004). Star-forming galaxies at high z should display a prominent discontinuity in $z - J$ while remaining blue in $J - H$, as illustrated in Fig. 3. The first issue we address is the optimum cut in both colors, on which depend both the redshift range explored and the amount of contamination by lower redshift objects.

Figure 3 shows color-redshift tracks for various galaxy classes (and also includes, for convenience, the colors of our eventual candidates discussed in §3.3). The location of these tracks suggests the following prescription for selecting sources with redshifts $6.8 \lesssim z \lesssim 8.0$:

$$(z_{850} - J_{110}) > 0.8; (z_{850} - J_{110}) > 0.66 (J_{110} - H_{160}) + 0.8; (J_{110} - H_{160}) < 1.2$$

The baseline $(z - J) > 0.8$ color selection we adopt above is similar to that used by Bouwens et al. (2004) and Bouwens et al. (2008). However, as the photometric errors for our candidates are typically 0.2-0.3 magnitudes, the probability of low-redshift contamination remains significant in the range $0.8 < (z - J) < 1.1$. Bouwens & Illingworth (2006) have also explored the use of a more restrictive color cut $(z - J) > 1.25$, also shown on Figure 3.

Concerning the J drop-outs, we adopt a cut of $(J - H) > 1.8$ corresponding to the redshift range $8.0 \lesssim z \lesssim 10.5$. Again, this is close to the cut adopted by Bouwens et al. (2005). In their shallower, larger area survey aimed at locating luminous J drop-out candidates, Henry et al. (2007) adopted a more restrictive $(J - H) > 2.5$ cut. Adopting this $J - H > 2.5$ cut would remove all our eventual J drop-outs from our sample (§3.3). However it must be remembered that the sample selected by Henry et al. is limited to NICMOS-detected sources in 2 bands only, with no deep supporting optical observations. Therefore, despite the apparent stringent color cut in $(J - H)$, it is still more likely to suffer from contamination by lower redshift sources.

We now turn to the important question of how complete our likely drop-out sample will be given our adopted magnitude limits with ACS and NICMOS. We can easily imagine that genuine drop-outs will be missed because photometric errors will scatter points outside our selection region; likewise, lower redshift sources will be scattered into our color selection box.

Using the procedures adopted to determine the 50% magnitude completeness limits in

Section 2.5, we can estimate the *color selection completeness* and *color selection contamination* by introducing artificial objects with a range of J magnitudes (AB=24 through 27) whose $z - J$ breaks have a range (0.6 through 1.2) and determining what fraction of truly low redshift objects end up in our box and what fraction of truly high redshift objects scatter out. We assume a flat f_ν spectrum for the UV continuum between the J and H bands so that, with reference to Figure 3, the problem becomes effectively one dimensional.

The two panels in Fig. 4 show the results of this test. The *selection completeness fraction* f_{comp} (left) represents the fraction of objects of a given magnitude and break color that we are able to recover in our selection. The *contamination fraction* f_{cont} (right) accounts for the fraction of objects with a lower break ($z - J < 0.8$) that are photometrically scattered in the color-color diagram so that their *observed* magnitude and color would allow them to enter our selection window. As with our magnitude completeness function, S_{comp} (§2.6), both of these correction factors will be used, for each candidate, to correctly estimate the true number density of objects having colors corresponding to $z > 6.8$ galaxies (i.e. a break $z - J$ above 0.8). Individual correction factors are reported in Table 5.

Examining Fig. 4, as expected we find negligible difficulties for the brightest sources, but contamination and incompleteness become more troublesome at fainter magnitudes, depending on the $(z - J)$ color. We find that the selection completeness ranges from 50-95%, with highest values 79% and 95% for the two best candidates satisfying the $z - J > 1.25$ color cut. The contamination fraction is typically 15%.

3.2. Verifying the Candidates

The selection techniques discussed above yields a list of candidates for more careful examination. Here we discuss further tests to determine the possibility that some might be spurious prior to establishing a catalog of genuine sources whose redshift distribution we will explore using our additional photometric data.

3.2.1. Spurious Detections

As the signature of both our z and J -band drop-outs consists of a non-detection in the optical band, we must seriously consider the possibility of spurious detections in the NICMOS data. This is particularly the case for the J drop-outs where only a single band is involved. An optical non-detection is defined as a implied flux lower than the photometric limit (5σ in a $0.3''$ -diameter aperture, for ACS and WFPC2 data, see Table 2). These

measurements were made using SExtractor in its “double-image” mode after the data was resampled and aligned to the NICMOS images. Further measures were made using the original multidrizzled images (see Sect. 3.5).

A visual inspection was performed for each candidate in order to reject obviously spurious detections in the NICMOS images or false non-detections in the optical bands. The astrometric position of the candidates was used to perform this examination on the original images, to prevent biases arising from resampling and geometrical transformations. During this process, we rejected a number of candidates due to their proximity to the center of the removed BCG, or due to obvious contamination from very bright galaxy haloes, both leading to noisier or biased photometric measurements.

Our photometric detection is based on the combination of 10 individual NICMOS images per pointing (4 and 6 exposures in the J_{110} and H_{160} band, respectively). Because of a significant number of remaining hot and dead pixels in these individual frames, we investigated the fraction of spurious sources that would contaminate our photometric catalogs. To quantify this problem, we constructed a *noise image* for each cluster and near-infrared band whose purpose is to remove signals from all genuine sources while maintaining the same noise properties as the real data. This was done by subtracting in pairs the individual frames prior to eventual coaddition. We then applied our usual photometric detection software, using the same parameters as in the original images.

This noise image reveals residuals near the frame edges (due to the dithering process undertaken during the observations) and in the centers of the brightest objects, which were masked out in the detection process (Figure 5). The affected area accounts, in total, for $\sim 20\%$ of the NICMOS field. By comparing the number of spurious sources detected in the noise image with the number of objects present in the original catalogs, we estimate the spurious fraction in the magnitude range of our candidates ($24.7 < J < 26.3$ and $25.3 < H < 26.7$) to vary from 4% to 18% from cluster to cluster, with an average value of 10%. Typically, therefore, we can expect around 90% of our candidates to be robust astronomical detections.

3.2.2. Detector Remnance

One specific worry, not addressed in the tests mentioned above, concerns the possibility of image persistence or ghosts appearing in the NICMOS frame during, or shortly after, an overexposure by a very bright source (Daou & Skinner 1997). The source producing the largest number of counts (~ 25000 ADU) in our dataset is a $J_{AB} = 17.9$ star in Abell 2390.

We do not detect any measurable electronic ghost for this particular source, but persistence is seen at the level of a $J_{AB} = 24.9$ spurious source in an exposure taken 20 minutes later. Once averaged over the entire sequence (6 exposures), this persistence corresponds to a $J_{AB} = 26.8$ source, i.e. fainter than our detection limit. We also verified, for each pair of successive exposures, that none of our candidates is coincidentally located at the relevant position of similarly bright ($J < 19$) stars in all clusters.

Although NICMOS exposures from independent orbits are usually separated by a > 30 minute delay, persistence might arise as a result of much brighter sources observed immediately prior to execution of our program. To eliminate this possibility, we located all preceding exposures and found no measurable persistence in our data, even in the case of a calibration program (GO 10726, PI: de Jong) aiming at measuring non-linearity effects by repeatedly saturating the NIC3 detector.

3.3. Catalog of Drop-out Candidates

As a result of our visual inspection of the initial candidate list selected according to the precepts of Section 3.1, we emerge with 10 candidate z drop-outs and 2 J drop-outs. As seen in Fig. 3 (right), 2 of the 10 z -dropouts satisfy the most restrictive color-selection $(z - J) > 1.25$. The photometric measurements for these are summarized in Table 5 and the relevant detection images are presented in Fig. 6. Following the tests described above we can expect over 90% of these to be genuine astronomical sources.

3.4. Redshift Estimation

We now turn to the important problem of contamination by lower redshift sources. We first use the spectral energy distribution (SED) of each candidate to estimate the individual photometric redshift. We then consider statistical arguments that can be applied to our entire candidate population.

3.4.1. Photometric Redshifts

As we have seen, the two color selection presented in Sect. 3.1 enables us to select high redshift galaxies with some confidence. However, we can use the multiwavelength data available for each source, including all upper limits arising from non-detections, in order to derive a *photometric redshift probability distribution*. To accomplish this, we used an up-

dated version of the photometric redshift software HyperZ (Bolzonella et al. 2000). Best-fit redshift distributions were computed using a standard SED procedure with a variety of templates, including empirical data (Kinney et al. 1996; Coleman et al. 1980) and evolutionary synthesis models (Bruzual & Charlot 2003). We searched the redshift range $0 < z < 10$, while reddening was kept as a free parameter ranging between $A_V = 0$ and 2 mag, assuming the Calzetti et al. (2000) law. The effect of Lyman forest blanketing is included following the prescriptions of Madau (1995).

This approach is only practical for the z drop-out candidates and the main results are presented in Fig. 6 (rightmost panels) where we overplot the best fit templates on each SED and present the redshift probability distribution $P(z)$, marginalized over the entire parameter space (templates and reddening). As has been found by many workers (Lanzetta et al. 1996; Richard et al. 2006), the likelihood function reveals two peaks with different relative intensities, the relative height of the lower redshift peak acting as a valuable measure of foreground contamination, as it is linked to the color degeneracy between high-redshift star-forming galaxies and lower redshift early-type or reddened objects.

Encouragingly, each candidate is more likely to be at high redshift and the probability of a foreground source is negligible for 4 out of our 10 sources. Integrated over all our candidates, we use $P(z)$ to compute the probability that each object lies beyond a redshift of 6, $\alpha_6 = P(z > 6.0)$, after normalizing $P(z)$ to unity over the redshift range $0 < z < 10$. We find α_6 values ranging from 0.46 to 0.91, with an average value of 0.65.

3.4.2. *Stacked Imaging*

As is evident from Table 5, the individual candidate SEDs are mostly restricted to detections in only one or two bands, with upper limits at other wavelengths. Although this precludes precise photometric redshift measures for each candidate, we can make further progress by combining data over several adjacent wavebands, and also by examining the average SED of the population to see if it is statistically consistent with that expected for a high redshift source.

Several of our clusters have ACS data in multiple bands (Abell 2218, CL1358, Cl0024) which we combined after aligning the images with integer ACS pixel shifts and normalization each to a constant signal to noise ratio. The depth of this combined image, covering the wavelength range 4500 - 8000 Å, is typically 0.6 to 1.0 magnitudes deeper than the individual bands. Yet in each of the 5 z drop-outs, no optical detection is seen, increasing our confidence level in the corresponding drop-outs.

We likewise generated stacked z , J and H images for all 10 z drop-outs, as well as a stacked K image for the 4 sources observed with MOIRCS. In this case, We selected a $10'' \times 10''$ region around each candidate, and averaged the data rejecting 20% of the outlier pixels. For 6 objects free from contamination from nearby objects, the same stacking procedure was performed in the 3.6 and 4.5 μm IRAC bands. The stacked images are presented in Fig. 7. No significant flux was detected in either the stacked MOIRCS or IRAC images.

Using the SExtractor parameters adopted for processing the individual images, an average SED was constructed for 3 populations depending on the availability of multi-band ACS, K band and IRAC imaging. The photometric properties of each are listed in Table 6 and the SEDs are shown in Fig. 8. These various stacked datasets offers a new opportunity to address the question of foreground contamination.

Using HyperZ, we fit these three SEDs exactly as described in Sect. 3.4.1. The optimal photometric redshift is consistent in each case (Fig. 9), with $z_{ph} = 7.35 \pm 0.07$, and a reduced χ^2 lower than 1. We also fitted the same SEDs, but now restricting the photometric redshift to the range $0 < z_{ph} < 3$. The best fit at low redshift is found at $z_{ph} = 1.75 \pm 0.03$, but with a much higher χ^2 , between 5 and 10. To the extent that the low redshift solutions are credible, they imply galaxies with typically ages of 500-700 Myrs and extinction values of $A_V \sim 1.0 - 1.4$.

One question that arises is whether the near-infrared $J - H$ color for our z drop-outs is consistent with expectations, and also with that of the other limited detections at high redshift (Bouwens et al. 2008). Using the stacked images, we find this color is typically very blue: $J_{110} - H_{160} \sim 0.0$. We define the rest-frame ultraviolet slope β as $f_\lambda \propto \lambda^{-\beta}$ between the restframe wavelengths 1500 and 2000 Å (Calzetti et al. 1994), and estimate the uncertainty in β for our sources either from the dispersion within the range of plausible redshifts (at $\pm 1 \sigma$), or by using the adopted photometric error bars in J and H . In both cases, we find a consistent value: $\beta \sim 2.8^{+0.05}_{-0.2}$. The mean slope is somewhat bluer than the average value of 2.0 ± 0.5 for a sample of i band drop-outs measured at $z \sim 6$ by Bouwens et al. (2006) but within the range of $\beta \sim 3.0$ found by Bouwens et al. (2004) in their sample of z drop-outs, and marginally consistent with $\beta \sim 2.5$ given for several objects by Bouwens & Illingworth (2006). In order to produce such a blue ultraviolet slope, the SED can only be fit by very young models (typically < 100 Myrs) with little or no reddening ($A_V < 0.1$).

3.4.3. Galactic Stars

Our next test for foreground contamination concerns the question of low mass Galactic stars. Various authors (Stanway et al. 2004; Bouwens et al. 2004) have pointed out the difficulty of using optical-near infrared colors to distinguish between cool stars and breaks arising from Lyman absorption at high redshift. L (Cruz et al. 2007) and T (Burgasser 2004) dwarfs exhibit metal and H₂O absorption features which produce features similar to the drop-out signature. Indeed, L and T dwarfs from the SDSS and 2MASS surveys (Knapp et al. 2004) lie well within our color-color selection region (Fig. 3, right).

In such circumstances, HST data has occasionally been used to evaluate whether the sources have half-light radii R_h consistent with being extragalactic objects (Stanway et al. 2004). However, this is not a definitive criterion as we already know that many spectroscopically-confirmed low luminosity high redshift sources are unresolved (Ellis et al. 2001). We measured R_h , defined as the radius enclosing half of the flux in the detection (NICMOS) images, and compared the values with that derived for bright not-saturated stars ($0.2''$). Figure 10 represents the location of our candidates in a R_h vs J_{AB} diagram, together with all other objects in our photometric catalog. Unfortunately, surface brightness dimming generates a cut-off at large values of R_h , which does not allow to distinguish resolved and unresolved sources at the faintest magnitudes. This is the case for 4 of the z -dropouts. At most we can say that 2 dropouts are unresolved, whereas 4 are resolved, including our two most promising candidates (Figure 3).

Noting the difficulty of separating stars from galaxies at these faint limits, a more practical approach is to examine the likely contamination statistically. Using simulations by Burgasser (2004), we computed the number of expected low-mass stars in the total area surveyed with NICMOS (7.7 arcmin^2), for all spectral types between L0 and T8, up to the extent of the thick disk (1 kpc). Assuming a slope $\alpha = 0.0$ for the mass function, consistent with recent observations by Metchev et al. (2007), we predict only 1.1 dwarf in our survey. A more pessimistic $\alpha = 0.5$ slope yields 1.5 stars. Thus, while there is undoubtedly some uncertainty surrounding these predictions, it does seem unlikely that cool Galactic stars represent a significant contaminant at such faint limits.

3.5. Magnification and Multiple Images

Our final test concerning the high redshift nature of our candidate drop-outs concerns their location within the image plane of the lensing cluster. A key question is whether any might be expected to be multiply-imaged as was the case, for example, for the object studied

by Kneib et al. (2004). Most of the area covered by our NICMOS observations lies within the region of high magnification ($\mu > 2.5$ mags) where multiple images may occur.

Using the mass models for each cluster (updated using Lenstool from those referenced in Table 1), we estimate the magnification of each drop-out based on its photometric redshift and location and examine the likelihood of any counter images as well as their predicted location and relative fluxes. The Bayesian optimization method incorporated in Lenstool also provides the uncertainties in these quantities.

In the majority of the cases (7 out of the 10 z drop-outs), the model predicts a pair of images with similar fluxes (within 0.2-0.4 magnitudes) straddling the critical line (Figure 11). Single images are expected in two other cases (CL1358z3 and A2667z1) and in the final case (CL1358z1), the objects sits on the predicted critical line, but is not expected to be viewed as a distinct pair at the finite angular resolution of NICMOS. These three cases are consistent with our observations. Considering the two J drop-outs, A2219j1 is predicted to be a further close merging unresolved by HST, and A2667j1 is predicted to have much fainter counter-images (by 0.8 to 1.5 mags) we do not expect to detect.

Our attention is thus focused on the 7 cases where second images are expected. The typical positional errors are around 1-3 arcsecs. Unfortunately, most are located outside the area surveyed by NICMOS or in regions close to the edge of the detector or under the central BCG where the noise level is high. Only in two cases, A2218z1 and A2667z2, does the mass model predicts a detectable counter-image in a relatively clean region of the NICMOS detector. Unfortunately, no significant flux, within the range expected, was seen at either position in the J-band of H-band image.

This test provides the only null result in our exhaustive quest to confirm the high redshift nature of our candidates. Although it applies to only two of our 10 z -band drop-outs, there is no reason if these two are at high redshift that we should not see the counter-image. Nor is there any reason to consider these two drop-outs as inferior to the remainder. However, an identical search for multiple images was performed under the assumption that each candidate is at a lower redshift, $z \sim 2$. In that case, we would expect counter-images at a different position, closer to the center of the cluster, symmetric to the lower redshift critical line. We detect no flux for any of the candidates either. However, we did recover a counter-image for one of our more marginal first cut J -drop candidate in Abell 2390 with $J-H = 1.5 \pm 0.3$ (Fig. 12). We subsequently eliminated this candidate and can now verify, from the location of the pair around the critical line, that this is a $z \sim 2$ object. This discovery clearly illustrates how predictions from the lensing model can discriminate low-redshift contaminants.

3.6. Summary

We now summarize the likely success rate of our survey in generating high redshift sources, concentrating on the z -band drop-outs. Of our ten sources, we find that at most one source is spurious and \simeq one is a Galactic star. Admittedly, about half of our candidates are unresolved, but we believe this is to be expected given the intrinsically faint limits we are probing with our lensing clusters. The various photometric redshift tests, for individual and stacked populations, suggests a 35% contamination for low redshift ($z \simeq 2$) sources. Taking every test into account, we conclude that 6 of our 10 sources are likely to be genuine $z > 6.8$ star forming galaxies. This includes two particularly convincing sources, A2219-z1 and A2390-z1, which are resolved and satisfy the more rigorous color cut in Figure 3.

4. Spectroscopic Follow-up

Although deep imaging with HST has delivered candidates whose photometric redshifts lie beyond $z \simeq 7$, to date there has been not a single spectroscopic confirmation despite heroic efforts. A case in point is the $z \simeq 6.8$ lensed system in Abell 2218 (Kneib et al. 2004) which was the subject of 9.2ks exposure with the LRIS optical spectrograph and a marathon 33ks exposure with the NIRSPEC infrared spectrograph. A marginal continuum was seen but no emission lines were detected. This contrasts with the successful detection of Lyman α in IOK-1 (Iye et al. 2006) in 31ks. The latter source has an implied star formation rate of $\simeq 10 M_{\odot} \text{ yr}^{-1}$ whereas the source in Abell 2218, when magnified, was expected to have an observed line flux equivalent to an unlensed system with a star formation rate of $2.6 \times 25 \simeq 50 M_{\odot} \text{ yr}^{-1}$. A tantalizing explanation for the non-detection of Lyman α in the object in Abell 2218 is preferential damping by neutral hydrogen in lower luminosity sources.

Recognizing the absence of Lyman- α emission in sources whose lensed star formation rates should otherwise render the line visible, we conducted an ambitious spectroscopic campaign at Keck for some of our candidates. We naturally hoped that we might also secure the first spectroscopic verification of a $z > 7$ source.

4.1. Observations

We used the Near InfraRed SPECTrograph (NIRSPEC, McLean et al. (1998)) on the 10 m Keck II Telescope to follow-up the majority of our candidates in the window 0.964–1.120 μm , corresponding to the redshift range 6.9–8.2 for the Lyman- α line (1216 \AA). Observations were conducted in several runs between January and September 2007 and we secured good

data for 7 z -band drop-outs in total (see Table 7). This included the two most promising candidates discussed earlier.

We used a $42''$ long and $0.76''$ wide slit, offering a resolving power of $R \sim 1500$ and used dithered exposures of 10 minutes each. We adjusted the dithering distance (in the range $3\text{--}8''$) in each case (third column of Table 7), to prevent overlap between a candidate and another bright source. Occasionally it was possible to observe two candidates simultaneously. For two candidates where we expect multiple images, the location of the expected counter-image (see Sect. 3.5) was used to optimize the slit positions (Figure 11).

The NIRSPEC spectra were reduced following the flat-fielding, sky-subtraction, distortion corrections and flux calibration procedures described by Stark et al. (2007b). These reduction techniques ensure an improved removal of the sky background by subtraction prior to resampling. We observed standard stars each night and used these to flux-calibrate the final spectra and determine the associated variance and hence the 5σ limiting line flux. Each position was observed for about 3.5 to 4 hours in total, yield a limiting line flux of $\sim 3 \times 10^{-18}$ erg cm $^{-2}$ s $^{-1}$ in regions of minimum OH contamination (Figure 13), assuming a line width of ~ 300 km s $^{-1}$, as measured in the well-studied lensed system by Ellis et al. (2001).

We inspected each reduced 2-D spectrum for faint emission lines at the position of the candidate and, where relevant, that of the counter-image. No significant signal was detected for any of the candidates

4.2. Implications

While the outcome of our spectroscopic campaign is certainly disappointing, the presence of strong OH lines in z -band means that our limiting Ly- α flux ($\sim 3 \times 10^{-18}$ erg cm $^{-2}$ s $^{-1}$) applies only across 50% of the observed wavelength range. Thus we would only expect partial success even if all of our sources had intense emission lines. Nonetheless it is informative to consider what the absence of any emission might mean given the star formation implied by our continuum detections. We can convert our flux limit into a rest-frame equivalent width using our HST photometry. For our candidates, we find a typical upper limit of $W_\lambda \sim 5 - 20$ Å .

Stanway et al. (2007) have recently studied a sample of faint Lyman- α emitters at $z \sim 6.0$ selected from their photometry to be i -band drop-outs. They found a tail of high values for the W_λ distribution compared to similar studies undertaken at $z \sim 3.0$ (Shapley et al. 2003). They attribute this evolution to a tendency for stronger line emission in intrinsically faint sources. 58% of their sample has $W_\lambda > 25$ Å rest-frame.

Assuming no evolution in this distribution from $z \sim 6$ to $z \simeq 7-8$, we would expect ~ 4 Lyman- α emitters in our spectroscopic campaign, prior to considerations of the OH spectrum. The probability that all 4 objects lie in a region of the spectrum contaminated by OH emission is thus $(0.5)^4 \sim 0.06$, which is very unlikely. Even if only 4 of the 7 candidates we examined were at high redshift (based on our statistical estimates given in §3), we should expect to detect the emission for $\simeq 3$ cases. Here there would be only a 12% probability of each one being occulted by OH emission.

Thus, as in the case of the $z \simeq 6.8$ source in Abell 2218, the absence of emission in 7 candidates is somewhat surprising. Assuming a significant fraction are at high redshift as discussed in §3, this may be an important indication of the evolution in the intergalactic medium above $z \simeq 6$. Regardless of the cause, it adds to the challenge of making progress in verifying high redshift candidates.

Reconciling the above with the abundance of intrinsically faint Lyman α emitters claimed by Stark et al. (2007b) is admittedly difficult. Should the bulk of the drop-out population at $z > 7$ continue to reveal no emission, this would suggest a moderate neutral fraction that would challenge the transparency of the IGM at $z \simeq 8-10$ implied by the presence of feeble Lyman α emitters. The enigma simply reinforces the importance of continuing to attempt the detection and verification of line emission in very faint sources.

5. Discussion

In the foregoing we have described a concerted effort to quantify the abundance of low luminosity star forming galaxies conducted in parallel to a similar spectroscopic campaign which has examined the abundance of $z \simeq 8-10$ Lyman α emitters (Stark et al. 2007b). That study claimed that if even a small fraction of the candidates is truly at high redshift, a significant contribution to reionization is provided by low luminosity galaxies. In a similar manner, recognizing the limitations of our small samples, we now examine the luminosity function at $z \simeq 7.5$ and the possible contribution that our lensed drop-out sources may make to cosmic reionization.

5.1. Number Densities and the Source Luminosity Function

The intrinsic area of sky (i.e. that in the source plane) covered by the NICMOS images is strongly dependent on the geometry of the critical lines (or caustics), which varies from cluster to cluster. Furthermore, multiple images occur in the central regions, duplicating the

corresponding source plane area. The result of both effects is a smaller survey, reduced by a typical factor of $\simeq 10$ in the source plane, with an increased depth whose value varies across the field of view.

In order to derive the source density of our z -band drop-outs, and to compare our results with those conducted in blank fields, we used the lensing models for each cluster to compute the sky area effectively observed in the source plane, down to a given intrinsic AB magnitude. We assumed our survey covers the image plane down to the measured 5σ depth $J_{110} \sim 26.2$ in the central NICMOS region, and scaled according to the relative exposure time near the edges. We also removed $\sim 10\%$ of the NICMOS area affected by bright galaxies. We supposed an average redshift of $z = 7.5$ to compute the magnification factors. Our total surveyed area is a factor ~ 5 smaller than the UDF in the same magnitude range ($AB < 27.7$, Fig. 14). However, the increased depth enables to reach $AB \sim 28 - 30$ in this area. A very similar result is found in the case of J -band drop-outs, assuming $z=9$.

We used the estimated color selection contamination factor, f_{cont} , and the selection completeness factor, f_{comp} (Sect. 3.1 and Table 5), to correct each z drop-out individually to derive intrinsic number densities. Because of the strong variations in the magnification factor across the NICMOS field of view, we corrected for observed completeness by computing the completeness factors in intrinsic (unlensed) $< J + H >$ magnitude. This combines both the observed completeness factor, S_{comp} , given in Table 2 and the surface reduction in the source plane. Error bars in the number densities were computed using Poisson noise estimates. We present the cumulative UV luminosity function of the z -band drop-outs in the magnitude range $27.0 < AB < 30.0$ in Fig. 15.

As discussed, we are confident that 6 out of our 10 sources are at high redshift. Accordingly, we evaluated two possible cases, presented in Fig. 15:

- (a) we randomly selected 6 sources from our sample 100 times in order to take into account object-to-object variations in the magnification factor and used this to estimate more realistic error bars,
- (b) we evaluated the surface densities from our 2 best candidates (A2219z1 and A2390z1) satisfying the most restrictive color selection criterion $(z - J) > 1.25$.

For comparison, we also overplot in Fig. 15 the luminosity function found by Bouwens et al. (2006) in the UDF, after correcting for redshift evolution between $z = 6.0$ and $z = 7.5$, as well as the best Schechter function fits recently claimed by Bouwens et al. (2008) from an analysis of their sample of z -band drop-outs. Not surprisingly, there is no overlap between these blank field measures and our, much deeper, lensed survey. All that can be said is that our results, which probe more than $\simeq 2.5$ magnitudes fainter are marginally consistent down

to AB \sim 28.5, and higher by $\sim 0.3 - 0.6$ dex at fainter luminosities.

5.2. Contribution to Cosmic Reionization

We finally investigate whether the likely abundance of low luminosity sources found in our survey could make a significant contribution to cosmic reionization. The approach we use is somewhat similar to the one described by Stark et al. (2007b), who estimated the comoving number density of sources necessary to keep the intergalactic medium (IGM) reionized under reasonable assumptions, and compare those to the abundances derived from candidate Lyman- α emitters at high redshift.

In our case, we can estimate the star formation rate density, measured in individual objects from their UV rest-frame luminosity, after applying the same completeness corrections described in Sect. 5.1. We converted the intrinsic (unlensed) $J + H$ magnitudes of our candidates into a UV luminosity, L_{1500} , and infer the related star formation rate (SFR) by adopting the Kennicutt (1998) calibration. All z -band drop-outs span the range $\text{SFR} \sim 0.1 - 1.0 M_{\odot} \text{ yr}^{-1}$, thus the overall star-formation rate observed yields the contribution of low star-formation rate sources to the entire star-formation rate density ρ_{SFR} .

We used the Madau et al. (1999) formalism to estimate the amount of star-formation necessary to keep the IGM reionized at a given redshift. One important factor in this calculation, that would modify the efficiency of star-forming sources to reionize the IGM, is the H_{II} clumping factor C , defined as $C = \langle n_{HII}^2 \rangle / \langle n_{HII} \rangle^2$ with n_{HII} being the density of ionized hydrogen. This factor measures the inhomogeneity of ionized hydrogen in the IGM which will likely increase between $z = 10$ and $z = 6$ due to the growth of structure. Assuming an IMF with a Salpeter slope with stellar masses ranging from $1 M_{\odot}$ to $100 M_{\odot}$, and a solar metallicity $Z=0.02$, the photon budget from star-forming sources necessary to reionize the IGM can be written as:

$$\dot{\rho}_{\text{SFR}} \simeq (0.031 M_{\odot} \text{ yr}^{-1} \text{ Mpc}^{-3}) \left(\frac{f_{\text{esc,rel}}}{0.5} \right)^{-1} \left(\frac{C}{10} \right) \left(\frac{1+z}{8.5} \right)^3 \quad (1)$$

where $f_{\text{esc,rel}}$ is the escape fraction of ionizing photons. We assumed an escape fraction $f_{\text{esc,rel}}=0.5$ in our calculations. However, values as low as $f_{\text{esc,rel}}=0.02$ have been measured in $z \sim 3$ galaxies by Shapley et al. (2006). Lower escape fractions would increase the amount of star formation necessary to reionize the Universe, so adopting $f_{\text{esc,rel}}=0.5$ gives us a lower limit on ρ_{SFR} . On the other hand, top-heavy IMFs and differences in metallicities would make galaxies produce more ionizing photons per star-formation rate, but this effect is less

significant than variations in $f_{esc,rel}$ and C . Bolton & Haehnelt (2007) have critically reviewed possible values for the clumping factor C . Many authors (Bunker et al. 2004; Bouwens et al. 2006) have assumed $C = 30$, but much lower values are predicted from radiative transfer simulations (Iliev et al. 2006 find $C < 2$ at $z > 11$).

Fig. 16 illustrates the star formation rate densities obtained by integrating down to a given SFR for the two extreme luminosity functions derived by Bouwens et al. (2008) when fitting their number densities at higher luminosities (equivalent to $SFR > 1.0 M_{\odot} \text{ yr}^{-1}$). We overplot on this figure the contributions derived from Eq. 1 with clumping factor varying between $C = 2$ and $C = 30$.

As suggested before, luminous galaxies do not produce enough star formation to reionize the IGM at these redshifts, even when a low $C = 2$ clumping factor is assumed. Lower luminosity galaxies are required to rescue the situation. Combining the source density from our NICMOS survey with those claimed at $SFR > 1.0 M_{\odot}$ estimated by integrating the luminosity function from Bouwens et al. (2008), we can compare the photon budget down to $SFR \sim 0.1 M_{\odot} \text{ yr}^{-1}$ with the amount of star-formation rate necessary to reionize the IGM. The results, shown in the case of 6 objects randomly chosen from our sample of 10 z -dropouts, or in the case of our 2 best candidates, suggest a contribution compatible with that necessary for reionization for clumping factors in the range $2 < C < 10$.

6. Conclusions

The overall goal of this project has been to constrain the abundance of low-luminosity star forming galaxies at $z \sim 7 - 10$, selected as z - and J -band drop-outs in the fields of 6 lensing clusters observed with ACS and NICMOS onboard the Hubble Space Telescope, and the IRAC camera onboard the Spitzer Space Telescope. We summarize our results as follows:

1. We have identified 12 promising high redshift candidates (10 z -band drop-outs and 2 J -band drop-outs) according to carefully-determined photometric selection criteria. These are located in 5 of the 6 clusters and span the observed magnitude range $J_{110} \simeq 25\text{-}26$. Each is typically magnified by 1.5 to 4 magnitudes.
2. Based on a comprehensive set of tests, we estimate the fraction of sources that might represent spurious detections and the extent to which low mass stars and low redshift interlopers may contaminate our sample. Collectively, these tests suggest that at least 6 of our 10 z drop-outs are likely high redshift $z > 6$ objects. Two of the candidates are particularly convincing.

3. By stacking the available ACS, NICMOS, ground-based K -band and IRAC images, we investigated further the averaged properties of our lensed z drop-outs. We find a UV spectral slope $\beta \sim 2.8_{-0.2}^{+0.05}$ similar to that of higher luminosity candidates from the UDF. Such a slope suggests a very young stellar population with little reddening and strengthens our case that the bulk of our candidates are high redshift sources.
4. We searched for possible counter-images for our candidates based on the most recent lensing models for each cluster. Unfortunately, our results are inconclusive. Many of the counter-images either lie outside our NICMOS field or are close to foreground sources. We fail to detect a counter-image in two apparently clean cases but a further two sources may be potentially merging on the critical line.
5. We undertook follow-up spectroscopy with NIRSPEC for 7 of our 10 z -band drop-out candidates in the hope of seeing confirmatory Lyman α emission. No emission was found in any candidate (or its counter-image location) to a flux limit corresponding to 3×10^{-18} ergs s $^{-1}$ cm $^{-2}$ in the clean part of the OH spectrum. One explanation is possible evolution in the Lyman- α rest-frame equivalent width distribution, compared to previous results by Stanway et al. (2007) at $z \sim 6$, such as might be expected if the neutral fraction rises with redshift. Such a deduction would be difficult to reconcile with the presence of intrinsically-faint lensed Lyman α emitters at $z \simeq 10$ Stark et al. 2007b
6. Our inferred luminosity function at $z \sim 7.5$, after correcting for contamination and incompleteness, is marginally consistent with an extrapolation of available constraints at brighter luminosities, with a slightly higher normalization by 0.3-0.6 dex. If even a modest fraction of our sources are at high redshift, our results strengthen the suggestion that sources with star formation rates $\sim 0.1 - 1.0$ M $_{\odot}$ yr $^{-1}$ contribute significantly to cosmic reionization.

As we approach the era of JWST and the ELTs, the outcome of our project in lensed fields has been to provide new constraints on the faint part of the luminosity function at $z > 7$, which confirmed the trends seen at higher luminosities. Despite being restricted to a small field after demagnification in the source plane, we expect that these results will be readily confirmed by the upcoming Wide Field Camera (WFC3) on HST, combining extremely sensitive infrared channels with a field of view much larger than NICMOS.

We acknowledge helpful discussions with Rycharde Bouwens, Rodger Thompson, Elizabeth Stanway, Roser Pelló, Daniel Schaerer, Kelle Cruz and Adam Kraus. Andrew Blain and Naveen Reddy kindly provided the Keck NIRC observations of Abell 2218. We are thankful

to Ichi Tanaka for his support in the reduction of MOIRCS imaging data. We acknowledge funding from NASA grant HST-GO-10504.01-A and Spitzer program GO-20439. The authors recognize and acknowledge the very significant cultural role and reverence that the summit of Mauna Kea has always had within the indigenous Hawaiian community. We are most fortunate to have the opportunity to conduct observations from this mountain. This program is based on observations made with the NASA/ESA Hubble Space Telescope, which is operated by the Association of Universities for Research in Astronomy, Inc., under NASA contract NAS 5-26555, and the Canada-France-Hawaii Telescope (CFHT), which is operated by the National Research Council of Canada, the Institut National des Sciences de l’Univers of the Centre National de la Recherche Scientifique of France, and the University of Hawaii.

REFERENCES

- Bardeau, S., Soucail, G., Kneib, J.-P., Czoske, O., Ebeling, H., Hudelot, P., Smail, I., & Smith, G. P. 2007, *A&A*, 470, 449
- Beckwith, S. V. W. et al. 2006, *AJ*, 132, 1729
- Bertin, E., & Arnouts, S. 1996, *A&AS*, 117, 393
- Bolton, J. S., & Haehnelt, M. G. 2007, *MNRAS*, 382, 325
- Bolzonella, M., Miralles, J.-M., & Pelló, R. 2000, *A&A*, 363, 476
- Bouwens, R. J., & Illingworth, G. D. 2006, *Nature*, 443, 189
- Bouwens, R. J., Illingworth, G. D., Blakeslee, J. P., & Franx, M. 2006, *ApJ*, 653, 53
- Bouwens, R. J., Illingworth, G. D., Franx, M., & Ford, H. 2008, *astro-ph/0803.0548*, 803
- Bouwens, R. J., Illingworth, G. D., Thompson, R. I., & Franx, M. 2005, *ApJ*, 624, L5
- Bouwens, R. J. et al. 2004, *ApJ*, 616, L79
- Bradley, L. D. et al. 2008, *astro-ph/0802.2506*
- Bruzual, G., & Charlot, S. 2003, *MNRAS*, 344, 1000
- Bunker, A. J., Stanway, E. R., Ellis, R. S., & McMahon, R. G. 2004, *MNRAS*, 355, 374
- Burgasser, A. J. 2004, *ApJS*, 155, 191

- Calzetti, D., Armus, L., Bohlin, R. C., Kinney, A. L., Koornneef, J., & Storchi-Bergmann, T. 2000, *ApJ*, 533, 682
- Calzetti, D., Kinney, A. L., & Storchi-Bergmann, T. 1994, *ApJ*, 429, 582
- Casertano, S. 2000, *AJ*, 120, 2747
- Choudhury, T. R., & Ferrara, A. 2007, *astro-ph/0703771*
- Coleman, G. D., Wu, C.-C., & Weedman, D. W. 1980, *ApJS*, 43, 393
- Covone, G., Kneib, J.-P., Soucail, G., Richard, J., Jullo, E., & Ebeling, H. 2006, *A&A*, 456, 409
- Cruz, K. L. et al. 2007, *AJ*, 133, 439
- Daou, D., & Skinner, C. 1997, in *The 1997 HST Calibration Workshop with a new generation of instruments* /edited by Stefano Casertano, Robert Jedrzejewski, Charles D. Keyes, and Mark Stevens. Baltimore, MD : Space Telescope Science Institute (1997) QB 500.268 C35 1997, p. 263., ed. S. Casertano, R. Jedrzejewski, T. Keyes, & M. Stevens, 263–+
- Dickinson, M., Giavalisco, M., & The Goods Team. 2003, in *The Mass of Galaxies at Low and High Redshift*, ed. R. Bender & A. Renzini, 324–+
- Egami, E. et al. 2005, *ApJ*, 618, L5
- Elíasdóttir, Á. et al. 2007, *astro-ph/0710.5636*, 710
- Ellis, R., Santos, M. R., Kneib, J., & Kuijken, K. 2001, *ApJ*, 560, L119
- Eyles, L. P., Bunker, A. J., Ellis, R. S., Lacy, M., Stanway, E. R., Stark, D. P., & Chiu, K. 2007, *MNRAS*, 374, 910
- Fazio, G. G. et al. 2004, *ApJS*, 154, 10
- Franx, M., Illingworth, G. D., Kelson, D. D., van Dokkum, P. G., & Tran, K.-V. 1997, *ApJ*, 486, L75+
- Henry, A. L., Malkan, M. A., Colbert, J. W., Siana, B., Teplitz, H. I., McCarthy, P., & Yan, L. 2007, *ApJ*, 656, L1

- Ichikawa, T. et al. 2006, in Presented at the Society of Photo-Optical Instrumentation Engineers (SPIE) Conference, Vol. 6269, Ground-based and Airborne Instrumentation for Astronomy. Edited by McLean, Ian S.; Iye, Masanori. Proceedings of the SPIE, Volume 6269, pp. 626916 (2006).
- Iliev, I. T., Mellema, G., Pen, U.-L., Merz, H., Shapiro, P. R., & Alvarez, M. A. 2006, MNRAS, 369, 1625
- Iye, M. et al. 2006, Nature, 443, 186
- Jullo, E., Kneib, J.-P., Limousin, M., Elíasdóttir, Á., Marshall, P. J., & Verdugo, T. 2007, New Journal of Physics, 9, 447
- Kashikawa, N. et al. 2006, ApJ, 648, 7
- Kennicutt, R. C. 1998, ApJ, 498, 541
- Kinney, A. L., Calzetti, D., Bohlin, R. C., McQuade, K., Storchi-Bergmann, T., & Schmitt, H. R. 1996, ApJ, 467, 38
- Knapp, G. R. et al. 2004, AJ, 127, 3553
- Kneib, J.-P., Ellis, R. S., Santos, M. R., & Richard, J. 2004, ApJ, 607, 697
- Kneib, J.-P. et al. 2003, ApJ, 598, 804
- Koekemoer, A. M., Fruchter, A. S., Hook, R. N., & Hack, W. 2002, in The 2002 HST Calibration Workshop : Hubble after the Installation of the ACS and the NICMOS Cooling System, Proceedings of a Workshop held at the Space Telescope Science Institute, Baltimore, Maryland, October 17 and 18, 2002. Edited by Santiago Arribas, Anton Koekemoer, and Brad Whitmore. Baltimore, MD: Space Telescope Science Institute, 2002., p.337, ed. S. Arribas, A. Koekemoer, & B. Whitmore, 337–+
- Komatsu, E. et al. 2008, astro-ph/0803.0547, 803
- Lanzetta, K. M., Yahil, A., & Fernández-Soto, A. 1996, Nature, 381, 759
- Limousin, M. et al. 2007, ApJ, 668, 643
- Loeb, A., & Barkana, R. 2001, ARA&A, 39, 19
- Madau, P. 1995, ApJ, 441, 18
- Madau, P., Haardt, F., & Rees, M. J. 1999, ApJ, 514, 648

- McLean, I. S. et al. 1998, in Presented at the Society of Photo-Optical Instrumentation Engineers (SPIE) Conference, Vol. 3354, Proc. SPIE Vol. 3354, p. 566-578, Infrared Astronomical Instrumentation, Albert M. Fowler; Ed., ed. A. M. Fowler, 566–578
- Metchev, S., Kirkpatrick, J. D., Berriman, G. B., & Looper, D. 2007, astro-ph/0710.4157, 710
- Oke, J. B. 1974, ApJS, 27, 21
- Richard, J. et al. 2007, ApJ, 662, 781
- Richard, J., Pelló, R., Schaerer, D., Le Borgne, J.-F., & Kneib, J.-P. 2006, A&A, 456, 861
- Ryan-Weber, E. V., Pettini, M., & Madau, P. 2006, MNRAS, 371, L78
- Shapley, A. E., Steidel, C. C., Pettini, M., & Adelberger, K. L. 2003, ApJ, 588, 65
- Shapley, A. E., Steidel, C. C., Pettini, M., Adelberger, K. L., & Erb, D. K. 2006, ApJ, 651, 688
- Shimasaku, K. et al. 2006, PASJ, 58, 313
- Smith, G. P., Kneib, J.-P., Smail, I., Mazzotta, P., Ebeling, H., & Czoske, O. 2005, MNRAS, 359, 417
- Songaila, A. 2004, AJ, 127, 2598
- Spergel, D. N. et al. 2007, ApJS, 170, 377
- Stanway, E. R. et al. 2007, MNRAS, 376, 727
- Stanway, E. R., Bunker, A. J., McMahon, R. G., Ellis, R. S., Treu, T., & McCarthy, P. J. 2004, ApJ, 607, 704
- Stark, D. P., Bunker, A. J., Ellis, R. S., Eyles, L. P., & Lacy, M. 2007a, ApJ, 659, 84
- Stark, D. P., Ellis, R. S., Richard, J., Kneib, J.-P., Smith, G. P., & Santos, M. R. 2007b, astro-ph/0701279
- Stark, D. P., Loeb, A., & Ellis, R. S. 2007c, astro-ph/0701882
- Swinbank, A. M., Bower, R. G., Smith, G. P., Smail, I., Kneib, J.-P., Ellis, R. S., Stark, D. P., & Bunker, A. J. 2006, MNRAS, 368, 1631
- van Dokkum, P. G. 2001, PASP, 113, 1420

Werner, M. W. et al. 2004, ApJS, 154, 1

Cluster	RA	Dec	z	Mass model	$N_{mult}(N_z)$
Abell 2218	16^h35^m	$+66^d13^m$	0.176	Elíasdóttir et al. (2007)	37 (26)
Abell 2219	16^h40^m	$+46^d22^m$	0.226	Smith et al. (2005)	14 (6)
Abell 2390	21^h53^m	$+17^d42^m$	0.228	Swinbank et al. (2006)	11 (5)
Abell 2667	23^h51^m	-26^d05^m	0.233	Covone et al. (2006)	10 (5)
Cl0024+16	00^h24^m	$+16^d54^m$	0.390	Kneib et al. (2003)	9 (5)
Cl1358+62	13^h58^m	$+62^d31^m$	0.328	Franx et al. (1997)	5 (3)

Table 1: Lensing Cluster Sample: N_{mult} : number of multiple images used in the lens model (N_z number with spectroscopic redshifts)

Cluster	Filter	Program	Date	Exp. time	Depth (5σ)	Completeness
A2218	ACS ₄₃₅	9717	Aug04	7048	27.74	
	ACS ₄₇₅	10325	Aug04	5640	27.95	
	ACS ₅₅₅	9717	Aug04	7048	27.79	
	ACS ₆₂₅	9717	Aug04	8386	27.93	
	ACS ₇₇₅	10325	Aug04	9285	27.73	
	ACS ₈₅₀	9292/9452/10325	Apr02/Aug02/Aug04	19630	27.32	
	NIC3 ₁₁₀	9452/10504	Apr03/Dec05	8446	26.26	25.93
	NIC3 ₁₆₀	9452/10504	Apr03/Dec05	10559	26.76	26.07
	NIRC _K		Jul02	7200	25.5	
	NIRC _K		Jul06	13620	25.9	
	MOIRCS _K		May07	18000	26.1	
	IRAC _{3.6}	83/20439	Dec03/Oct05/Dec05	37700	25.5	
	IRAC _{4.5}	83/20439	Dec03/Oct05/Dec05	37700	25.5	
A2219	WFPC2 ₇₀₂	6488	Aug99	14400	27.00	
	ACS ₈₅₀	10504	Apr06	8374	26.75	
	NIC3 ₁₁₀	10504	May06/Jun06/Jun07	9216	26.23	25.97
	NIC3 ₁₆₀	10504	May06/Jun06/Jun07	11519	26.73	26.14
	NIRC _K		Jul06	22980	26.3	
	MOIRCS _K		Aug06	17550	26.1	
	IRAC _{3.6}	83	Feb04/Mar05	2400	23.9	
	IRAC _{4.5}	83	Feb04/Mar05	2400	23.9	
A2390	WFPC2 ₅₅₅	5352	Dec94	8400	26.6	
	WFPC2 ₈₁₄	5352	Dec94	8400	26.2	
	ACS ₈₅₀	9292/10504	May02/May06	8847	26.82	
	NIC3 ₁₁₀	10504	Jun06/Jul06/Jun07	9470	26.27	25.89
	NIC3 ₁₆₀	10504	Jun06/Jul06/Jun07	11839	26.54	26.06
	MOIRCS _K		May07	15900	26.0	
	IRAC _{3.6}	83	Jun04/Nov04	2400	23.9	
	IRAC _{4.5}	83	Jun04/Nov04	2400	23.9	
A2667	WFPC2 ₄₅₀	8882	Oct01	9600	26.26	
	WFPC2 ₆₀₆	8882	Oct01	4000	26.94	
	WFPC2 ₈₁₄	8882	Oct01	4000	26.11	
	ACS ₈₅₀	10504	Jul06	8765	26.70	
	NIC3 ₁₁₀	10504	Aug06	9343	26.22	25.93
	NIC3 ₁₆₀	10504	Aug06	11711	26.51	26.01
	IRAC _{3.6}	83	Dec03	2400	23.9	
	IRAC _{4.5}	83	Dec03	2400	23.9	
CL0024	ACS ₄₃₅	10325	Nov04	6435	27.67	
	ACS ₄₇₅	10325	Nov04	5072	27.81	
	ACS ₅₅₅	10325	Nov04	5072	27.47	
	ACS ₆₂₅	10325	Nov04	8971	27.75	
	ACS ₇₇₅	10325	Nov04	10144	27.67	
	ACS ₈₅₀	10325	Nov04	16328	27.28	
	NIC3 ₁₁₀	10504	Aug06	9472	26.20	25.9
	NIC3 ₁₆₀	10504	Aug06	11840	26.60	26.0
	MOIRCS _K		Aug06	21600	26.1	
	IRAC _{3.6}	64	Dec03	2400	23.9	
	IRAC _{4.5}	64	Dec03	3600	24.1	

Table 2: Imaging Data:.. For a given cluster each entry presents the instrument, filter, HST/Spitzer program ID, date of observation, exposure time, and final image quality (depth

Cluster	Filter	Program	Date	Exp. time	Depth (5σ)	Completeness
CL1358	ACS ₄₃₅	9717	Apr04/May04	5440	27.70	
	ACS ₄₇₅	9717	Apr04/May04	5470	27.96	
	ACS ₆₂₅	9717	Apr04/May04	6800	27.77	
	ACS ₇₇₅	9717	Apr04/May04	10144	27.49	
	ACS ₈₅₀	9717	Apr04/May04	16328	27.13	
	NIC3 ₁₁₀	10504	Dec05	9216	26.34	25.92
	NIC3 ₁₆₀	10504	Dec05	11519	26.60	26.10
	IRAC _{3.6}	83	Jan04/Jun05	2400	23.9	
	IRAC _{4.5}	83	Jan04/Jun05	2400	23.9	

Table 3: 2 (continued)

Cluster	Filter	Exposure Time	Seeing
A2219	B	5400	1".0
	R	6300	0".8
	I	3000	0".8
A2390	B	2799	1".1
	R	5700	0".7
	I	3600	0".9

Table 4: Additional CFHT optical data (Bardeau et al. 2007)

Candidate	R.A.	Dec.	z_{850} (AB)	J_{110W} (AB)	H_{160W} (AB)	K (AB)	$\mu(mags)$	S_{comp}	f_{cont}	f_{comp}
A2218-z1	248.9713	+66.2071	> 27.32	26.1±0.13	25.9±0.11	> 25.7	1.9	0.59	0.14	0.66
A2218-z2	248.9507	+66.2150	> 27.32	26.2±0.18	26.0±0.11	> 25.7	2.7	0.50	0.19	0.72
A2219-z1	250.0803	+46.7071	26.3 ± 0.15	24.7±0.05	25.3±0.06	> 25.7	3.6	0.84	0.0	0.95
A2390-z1	328.4130	+17.6905	> 26.82	25.5±0.12	26.1±0.12	> 25.6	3.5	0.68	0.17	0.79
A2390-z2	328.4001	+17.6962	> 26.82	25.8±0.15	25.8±0.10	> 25.6	1.8	0.65	0.27	0.51
A2667-z1	357.9119	-26.0949	26.7 ± 0.36	25.9±0.15	26.1±0.18	N/A	1.6	0.59	0.34	0.51
A2667-z2	357.9153	-26.0826	26.7 ± 0.42	25.7±0.12	25.6±0.11	N/A	2.0	0.75	0.20	0.68
CL1358-z1	209.9714	+62.5128	> 27.33	26.3±0.17	26.1±0.12	N/A	1.9	0.43	0.15	0.63
CL1358-z2	209.9521	+62.5108	> 27.33	26.2±0.13	26.7±0.28	N/A	4.0	0.43	0.15	0.72
CL1358-z3	209.9549	+62.5187	> 27.33	26.3±0.17	26.6±0.19	N/A	4.0	0.35	0.14	0.66
A2219-j1	250.0900	+46.7040	> 26.7	> 26.3	24.5±0.05	> 25.7	4.0			
A2667-j1	357.9136	-26.0869	> 26.7	> 26.5	24.6±0.08	N/A	3.6			

Table 5: High Redshift Candidate Photometry: total magnitudes and corresponding magnification assuming $z = 7.5$ for z -band drop-outs and $z = 9.0$ for J -band drop-outs. Each z drop-out entry is followed by its selection contamination factor, observed completeness and selection completeness

Dropouts	z_{850LP}	J_{110W}	H_{160W}	K	IRAC $_{3.6\mu m}$	IRAC $_{4.5\mu m}$
(all 10)	28.59 ± 0.21	25.72 ± 0.14	25.70 ± 0.14			
(all 4 with K-band)	28.99 ± 0.32	25.71 ± 0.14	25.81 ± 0.12	> 26.2		
(all 6 with IRAC)	29.10 ± 0.23	26.11 ± 0.16	26.29 ± 0.16		> 25.0	> 24.8

Table 6: Stacked Photometry of the z -band drop-outs

Run	Candidate(s)	Dither	Exposure Time	Seeing	Notes
Jan 2007	CL1358z1 and z2	$3''$	$9 \times 600s$	$0.5''$	
May 2007	CL1358z1 and z2	$3''$	$15 \times 600s$	$0.5\text{-}0.6''$	
	A2219z1	$5''$	$13 \times 600s$	$0.5\text{-}0.8''$	
			$12 \times 600s$	$0.5''$	
	A2218z1	$5''$	$18 \times 600s$	$0.9''$	candidate + counter-image
			$13 \times 600s$	$0.5''$	
	A2390z1	$5''$	$4 \times 600s$	$0.8''$	
Sep 2007			$12 \times 600s$	$0.5''$	
	A2390z2	$8''$	$21 \times 600s$	$0.5''$	candidate + counter-image
	A2667z1	$6''$	$17 \times 600s$	$0.5''$	

Table 7: Log of the spectroscopic observations performed on 7 of the z band drop-outs. From left to right: epoch of observation, candidate name, spatial dithering between individual exposures, exposure time, seeing conditions. For two z drop-outs, we managed to observe the predicted location of the counter-image at the same time as the candidate.

Ref.	z	Φ^* (Mpc $^{-3}$)	M^* (mag)	α
Bouwens et al. (2006)	6	$1.4e\text{-}3$	-20.25	-1.73
Bouwens et al. (2008)	7.4	$1.1e\text{-}3$	-19.80	-1.74
		$1.78e\text{-}3$	-19.60	-1.4
		$8e\text{-}4$	-19.90	-2.0

Table 8: Best-fit Schechter parameters of the high redshift UV luminosity function, from earlier results found in the UDF, and overplotted in Fig. 15. For each work we give the normalization Φ^* , the absolute magnitude M^* at the exponential cutoff and the faint-end slope α . Bouwens et al. (2008) explore three possible evolutions of the L^* and Φ^* parameters for different fixed slopes α .

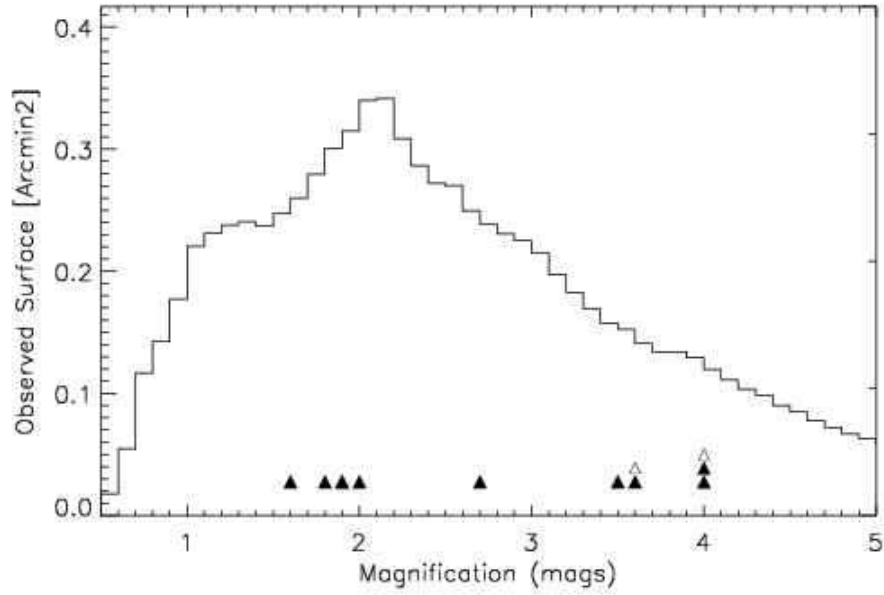


Fig. 1.— Distribution of magnification factors μ (in magnitudes) for the survey, as predicted from the mass models assuming a point source at very high redshift ($z > 7$). The vertical axis represents the observed surface area in each 0.1 mag (0.04 dex) magnification bin. The peak of this distribution indicates our typical magnification factor is ~ 2.0 mags. Filled triangles mark the individual magnification factors for the 10 z drop-out and open triangles that of the J drop-out candidates.

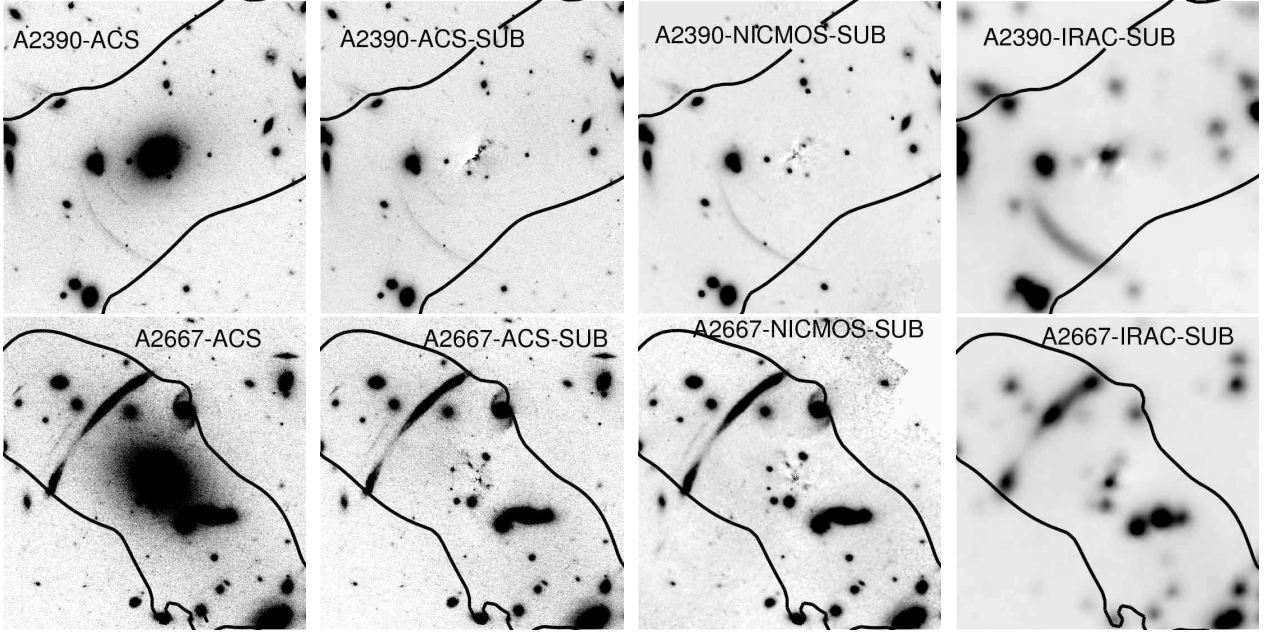


Fig. 2.— Example of BCG subtraction in the clusters A2390 and A2667. Each panel is $45''$ on a side. (Left to right): ACS image without subtraction, BCG-subtracted images in ACS, NICMOS and IRAC respectively. Subtraction residuals appear within ~ 1 arcsec of the center in the ACS and NICMOS case, ~ 2 arcsec for IRAC. The critical line for a high redshift source is shown by the black curve.

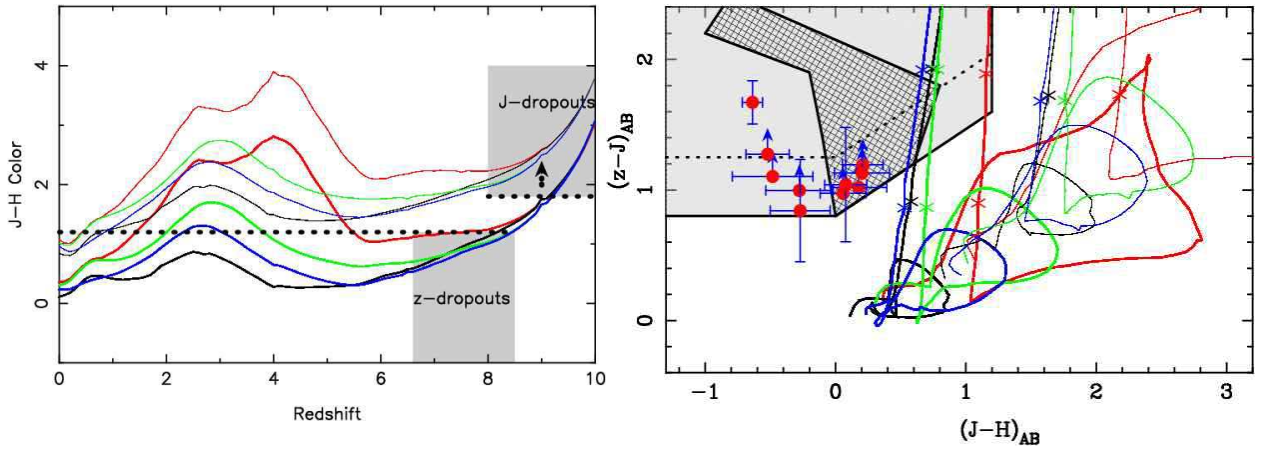


Fig. 3.— (Left) Optimizing the selection of high redshift z -band and J -band drop-out candidates using near-infrared colors (dotted lines) as compared to the expected colors of Hubble sequence galaxies (colored tracks) (Coleman et al. 1980; Kinney et al. 1996). Thick tracks assume no extinction, thin lines show the effect of including a selective extinction of $A_V = 1.0$ magnitudes. (Right) Color-color diagram used for selecting high redshift z -band drop-out candidates. The final set of candidates is presented in red (see §3.3). Color tracks represent predicted colors for Hubble sequence galaxies (as in left panel). The observed location of L and T dwarfs is shown as a cross-hatched region (Knapp et al. 2004). Two possible $z - J$ color selections (> 0.8 and > 1.25) are shown (see text for details).

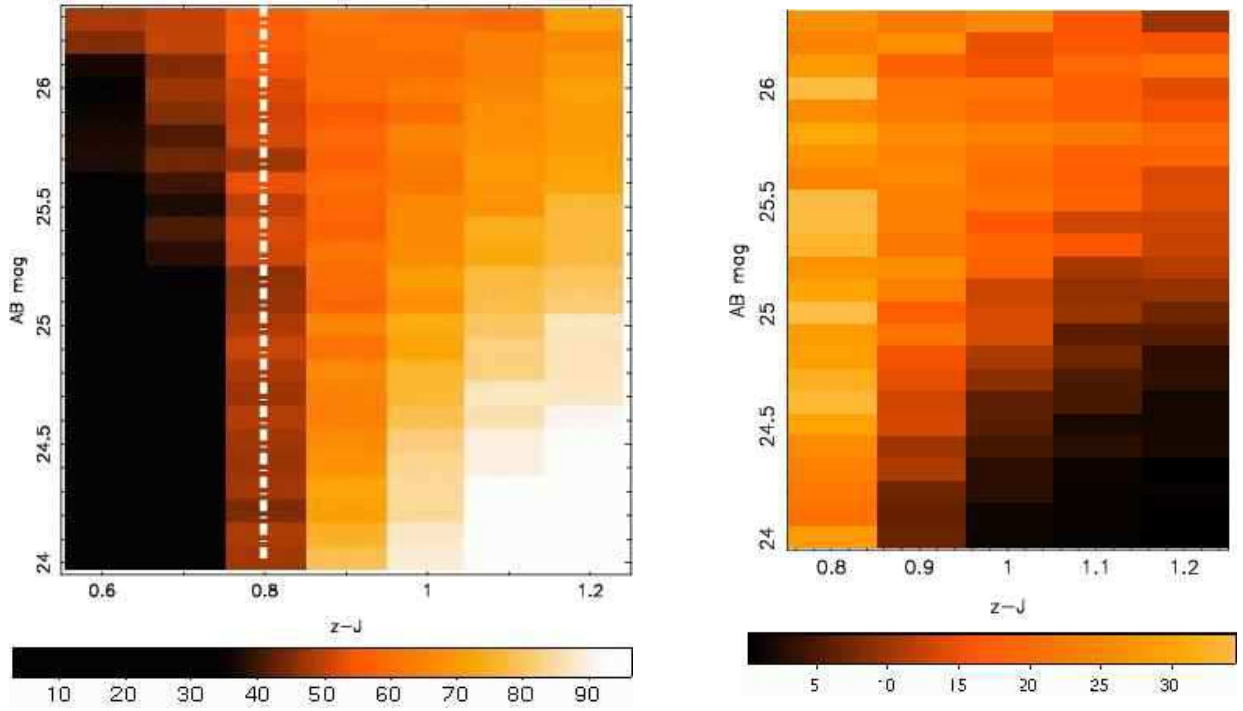


Fig. 4.— Testing the color-selection of z -band drop-outs. (Left) Completeness in the color-selection (f_{comp}), as a function of the J or H magnitude (assuming a flat spectrum in AB) and the $(z - J)$ color-break. Values represent the fraction (%) of simulated objects whose photometry satisfies our color-selection criteria as indicated in the color bar beneath. (Right) As for the left panel but referring to the contamination fraction f_{cont} .

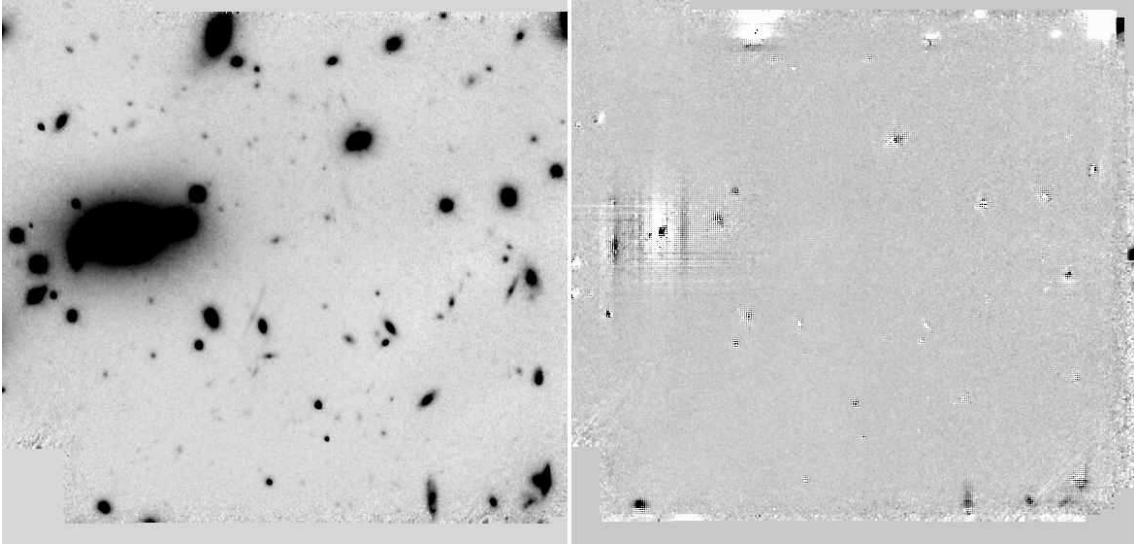


Fig. 5.— NICMOS image of the cluster CL1358 (left) compared with a noise image (right) in order to estimate the fraction of spurious sources in our sample (see text for details). Except in the vicinity of the edges and central cores of bright objects (which are masked out by applying a simple threshold), the noise properties of the two images are very similar.

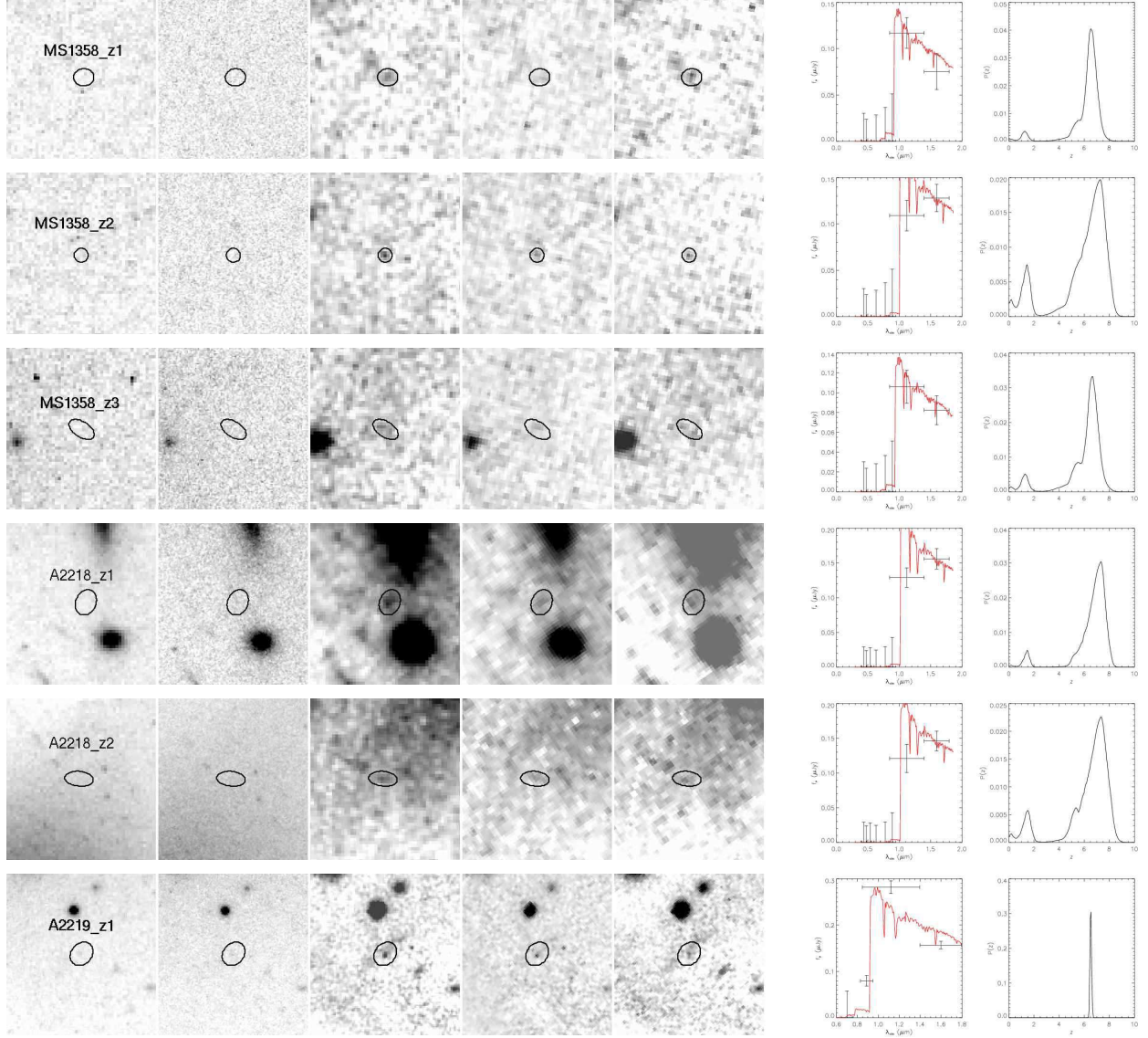
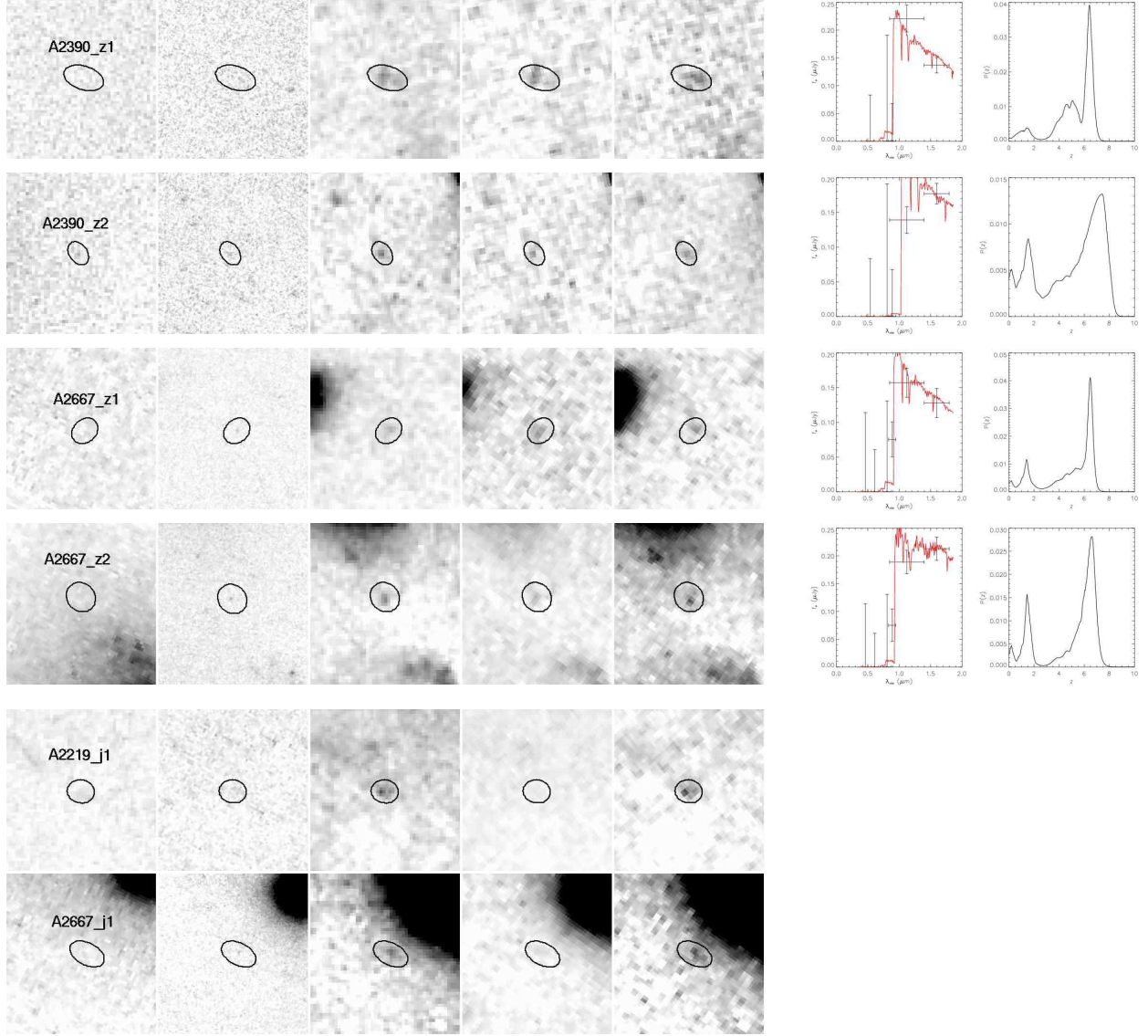
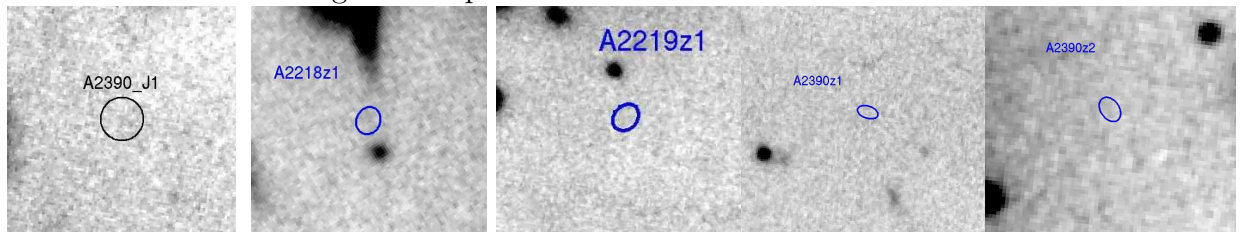


Fig. 6.— Snapshot images our final catalog of candidate drop-outs. (Left to right): HST images in the optical (ACS or WFPC2), in the ACS/F850LP (z) band, in the detection image (sum of F110W and F160W bands), in the NIC3/F110W and the NIC3/F160W images. To the right are the observed SED with the overplotted best fit template for HyperZ, and the redshift probability distributions (see Sect. 3.4.1). Shown separately are the MOIRCS *K* band images.).



MOIRCS - K -band images of drop-outs



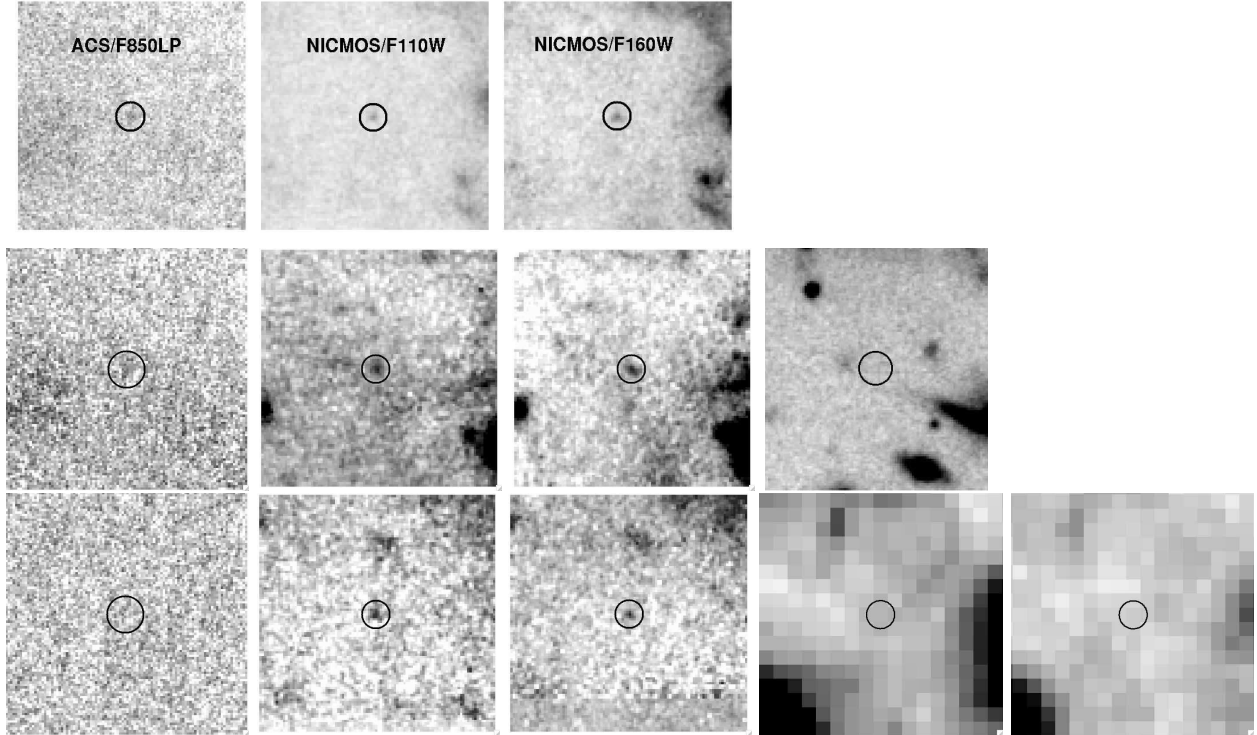


Fig. 7.— Stacked images of the z -band drop-outs. First row: ACS and NICMOS images of all 10 sources. Second row: stacked images for the 4 drop-outs with K -band imaging (rightmost image). Third row: stacked images for those 6 sources with unconfused IRAC data.

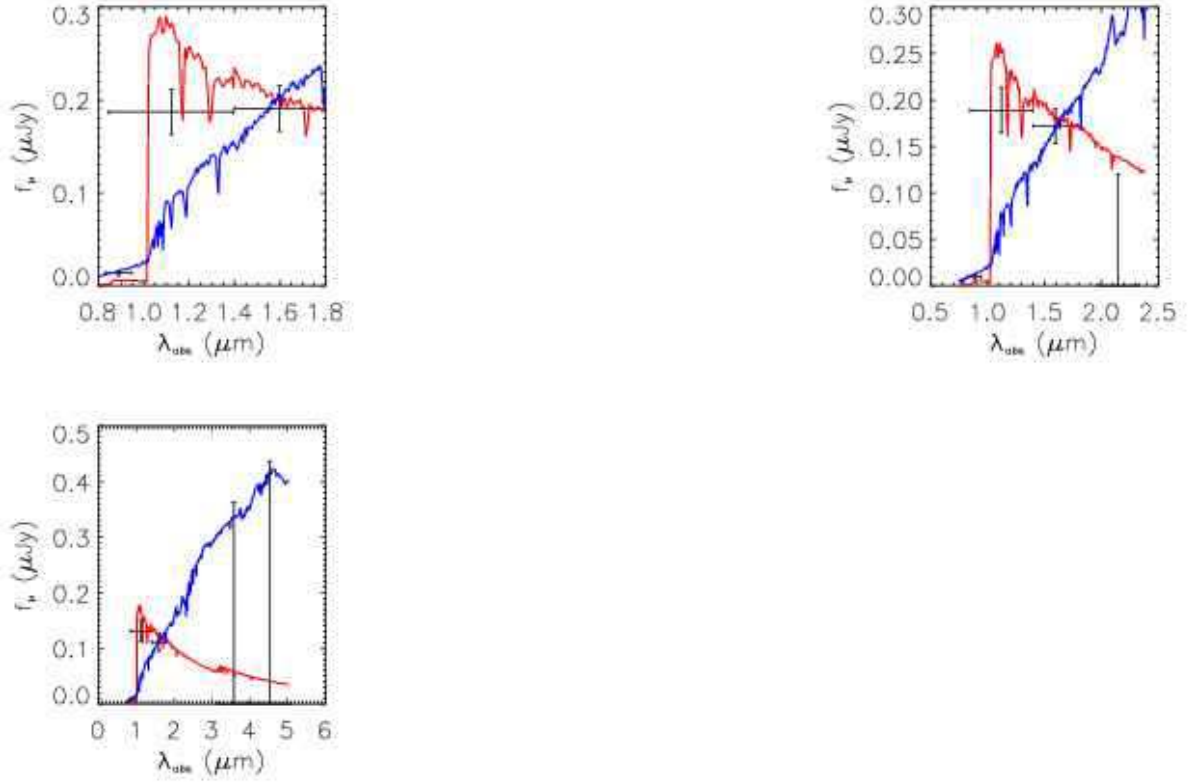


Fig. 8.— SED of the z -band drop-outs derived from the stacked photometry (see Fig. 6). (Left to right): all 10 drop-outs with ACS/NICMOS data, drop-outs with useful ACS/NICMOS/MOIRCS data, drop-outs with useful ACS/NICMOS/IRAC data. In each case, the best template found with HyperZ over $0 < z < 10$ (red curve) or $0 < z < 3$ (blue curve) is shown.

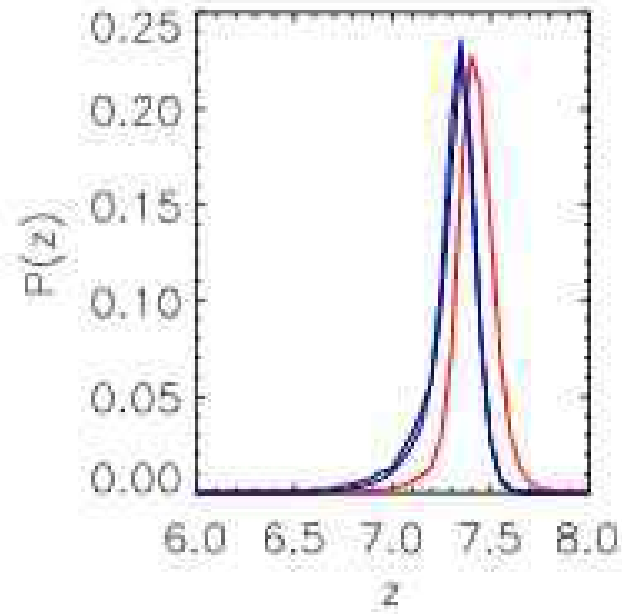


Fig. 9.— Redshift probability distribution estimated using HyperZ for the stacked SEDs of the z -band drop-outs shown in Fig. 8. The black, red and blue curves refer respectively to all 10 dropouts, those four with K -band imaging, and those 6 sources with useful IRAC upper limits. All three solutions are consistent with a mean population redshift of $z \sim 7.35$.

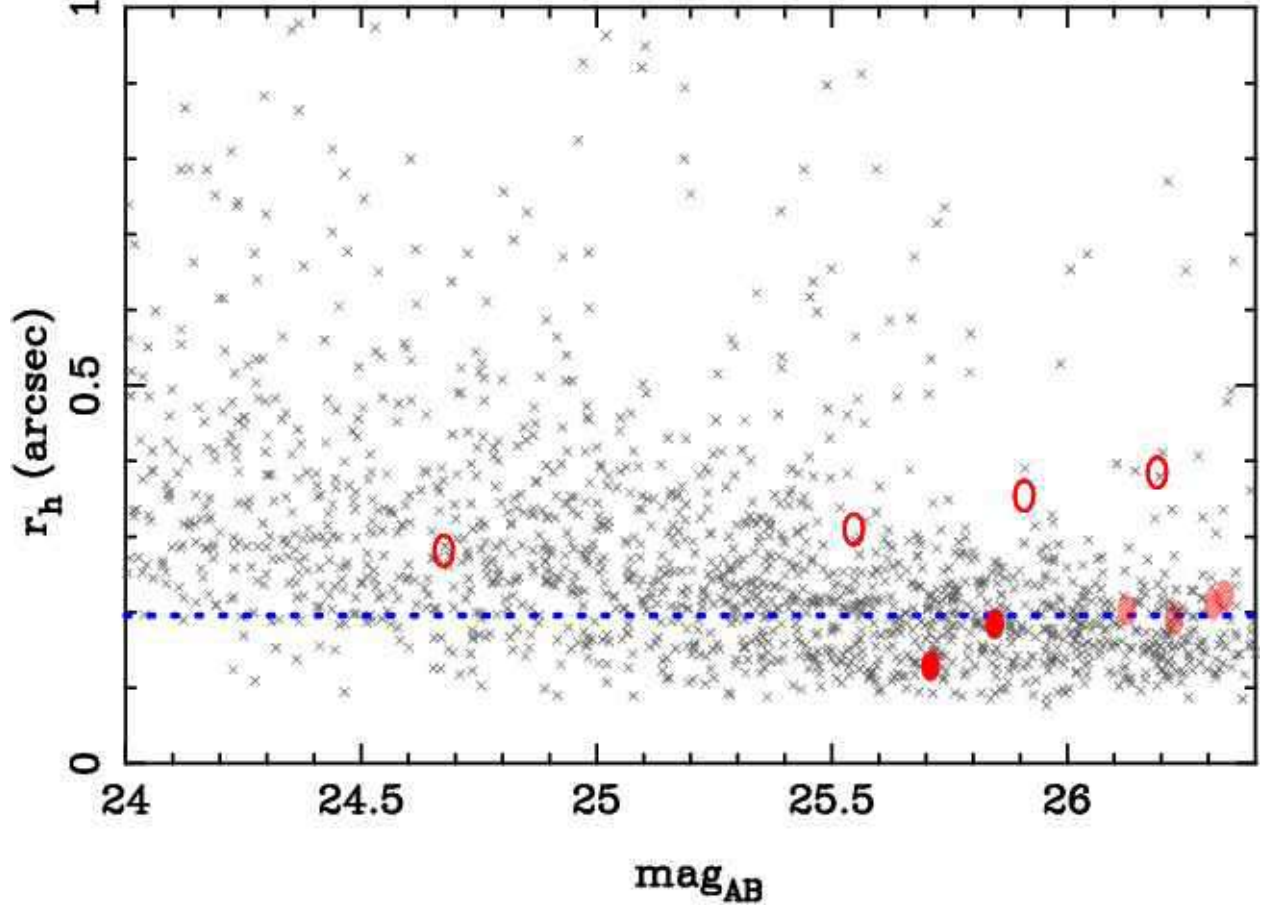


Fig. 10.— Distribution of half-light radii r_h measured by SExtractor in the photometric catalogs, as a function of the total J band magnitude. The blue dashed curve corresponds to the measured r_h for bright non-saturating stars. The 10 z -band drop-outs are shown as red ellipses. Two objects are unresolved (filled ellipses) whereas four appear resolved (open ellipses.). The rest cannot be reliably categorized.

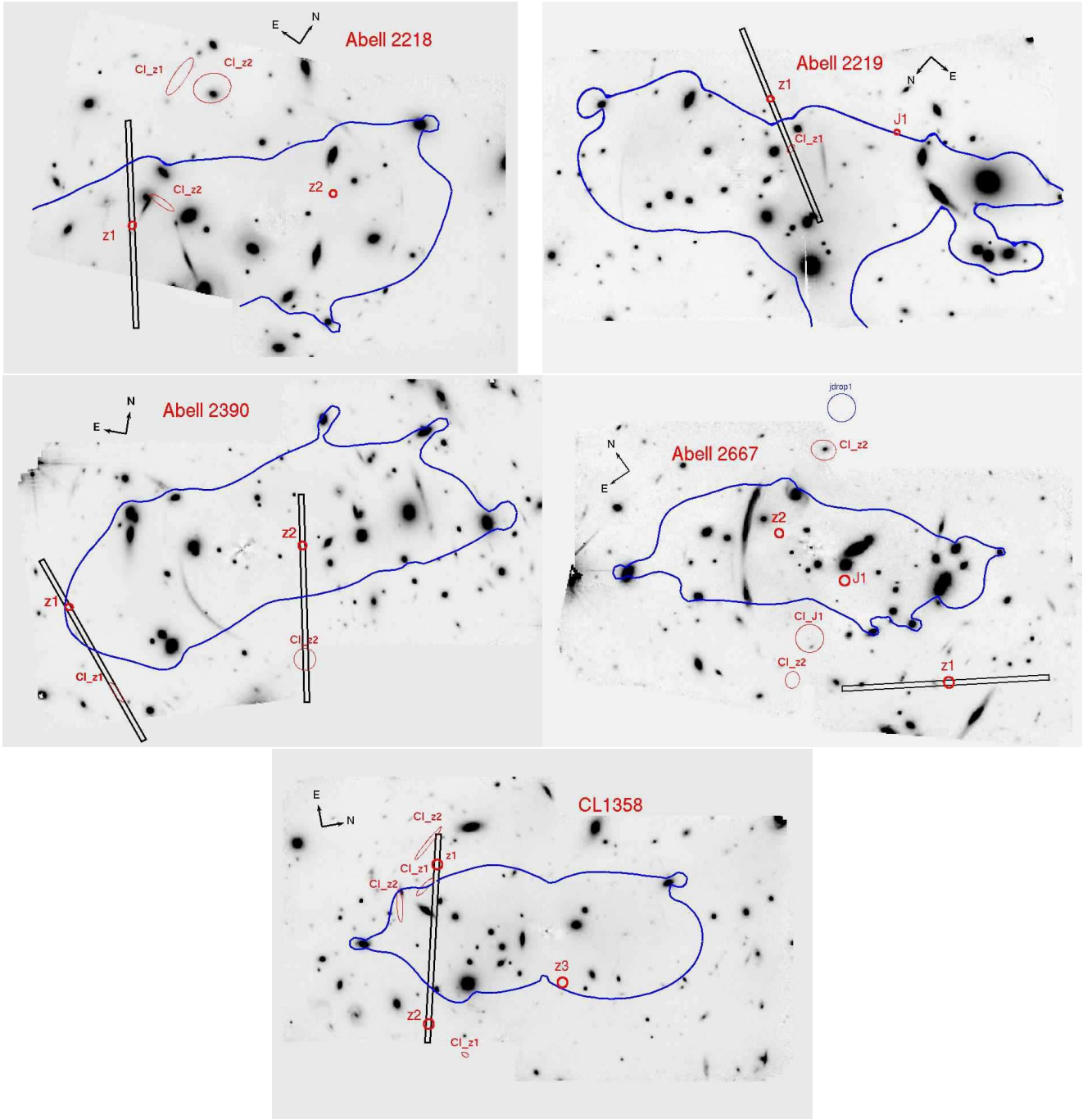


Fig. 11.— Location of the z -band and J -band drop-outs with respect to the high redshift ($z = 7.5$) critical line for each cluster field (blue curve). Ellipses with a “CI” label mark the position (and estimated error) of the brightest counter-images. The adopted NIRSPEC follow-up slit position angles are overplotted as black rectangles.

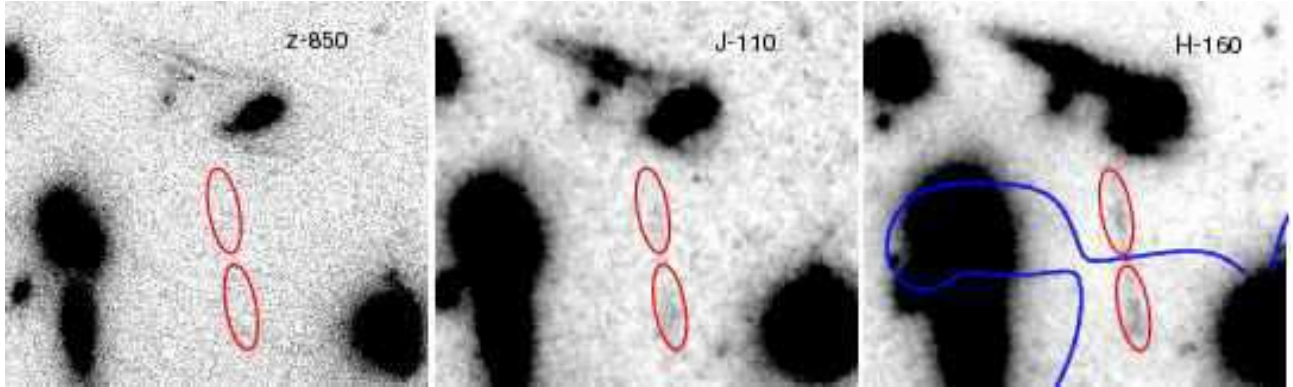


Fig. 12.— A pair of magnified optical drop-outs identified in the NICMOS images. The theoretical location of the $z = 1.8$ critical line (right panel) confirms this source to be a low- z contaminant.

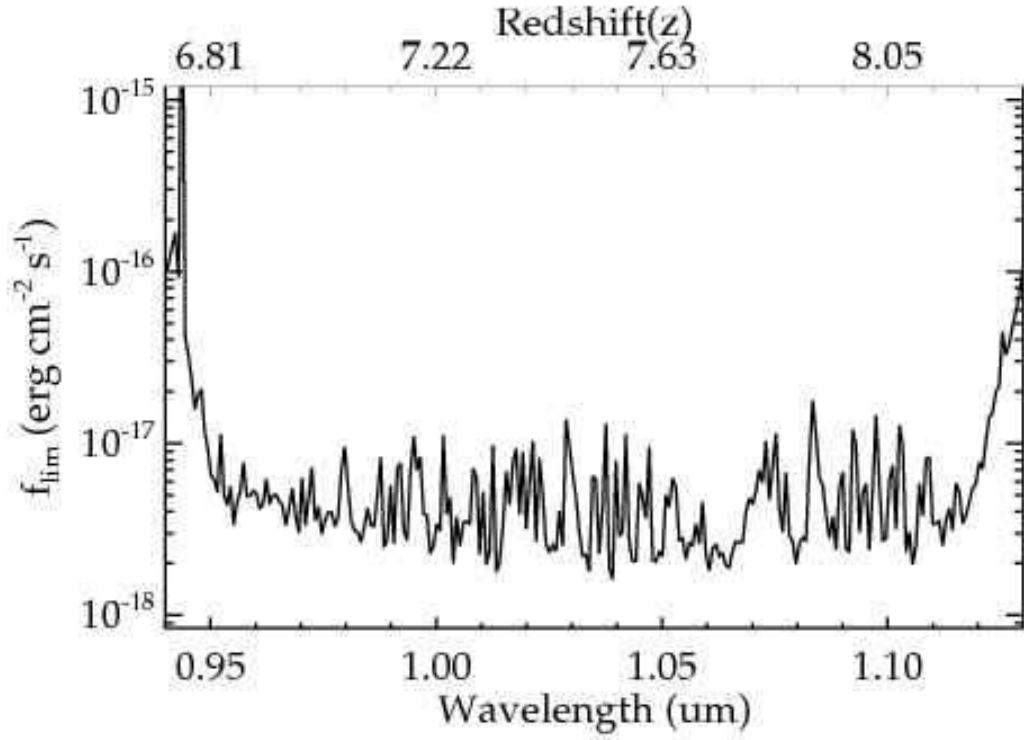


Fig. 13.— Determining the limiting flux from the NIRSPEC follow-up campaign. The plot shows the 5σ limiting emission line flux versus wavelength (and inferred Lyman α redshift) for a typical 3.5 hours integration.

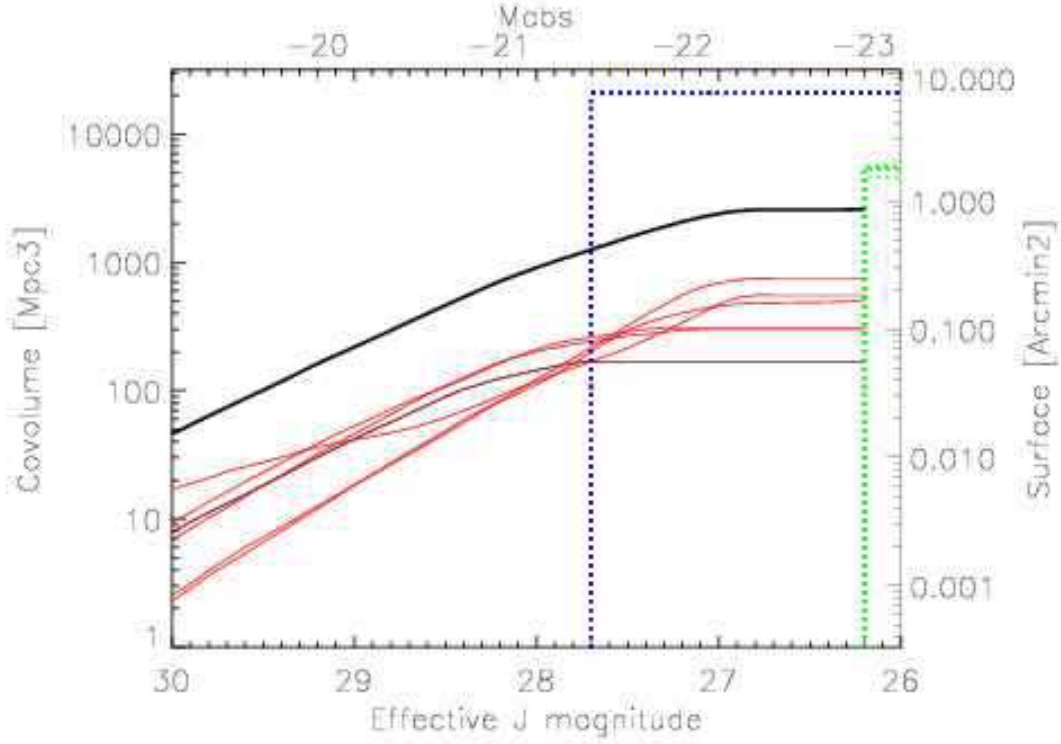


Fig. 14.— Survey characteristics: the intrinsic (unlensed) surface area sampled in the source plane down to a given limiting magnitude for each cluster (thin red lines) and for all six clusters (thick black line). The green dashed lines illustrate the areas sampled in the absence of lensing. The blue dotted line shows the equivalent survey parameters for the UDF (Bouwens et al. 2004; Bouwens & Illingworth 2006).

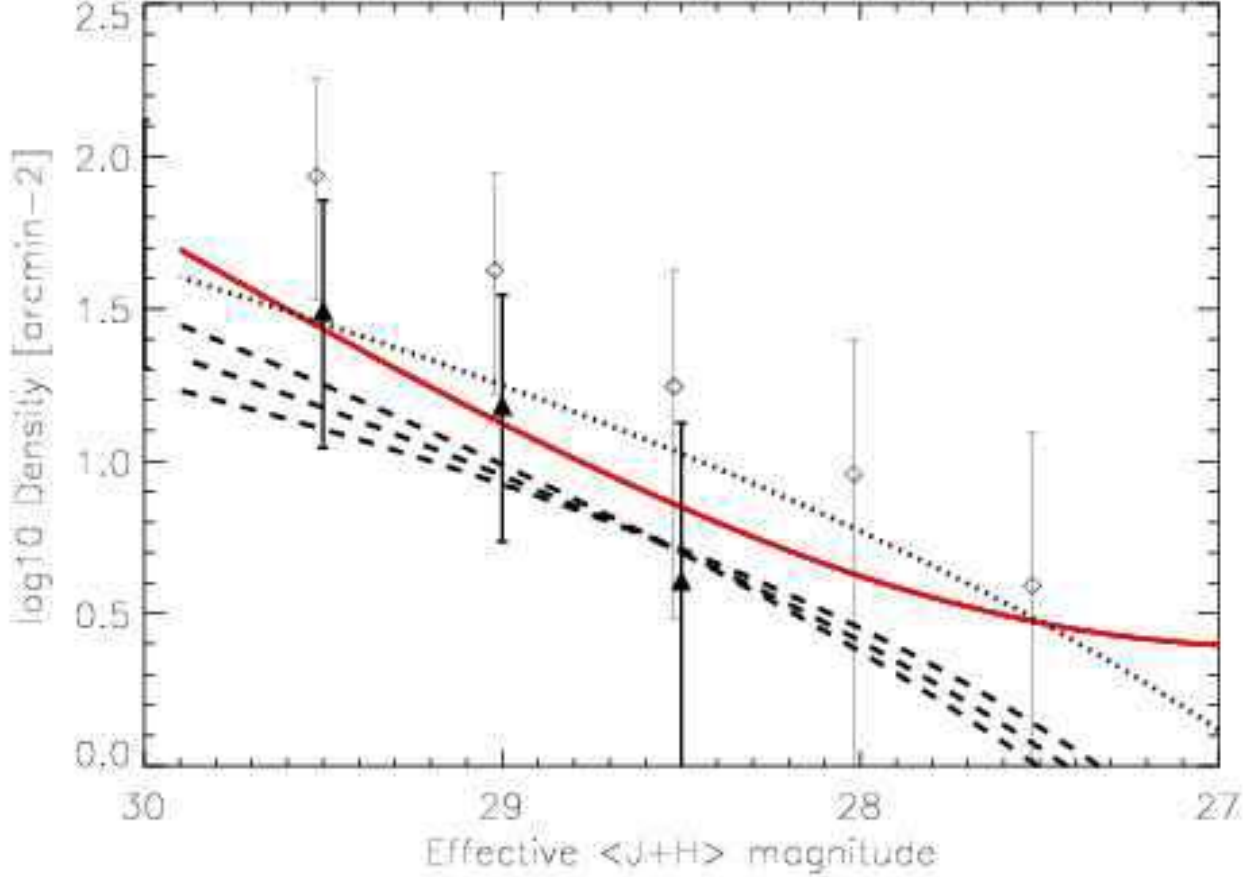


Fig. 15.— The cumulative number density of star-forming galaxies at $z \sim 7-8$ as a function of the effective (unlensed) magnitude. Datapoints and error bars correspond to the range of densities resulting when (a) randomly selecting 6 candidates from our sample and adopting Poisson errors (open diamonds, offset for clarity), or (b) restricted to the two most promising candidates satisfying the $(z - J) > 1.25$ selection criterion (filled triangles). In the most pessimistic case, where no sources are at high redshift, the implied upper limit is shown by the thick red curve. We overplot the best fit luminosity functions found by Bouwens et al. (2006) (light dotted line) and Bouwens et al. (2008) (bold dashed lines) in the UDF (parameters in Table 8)

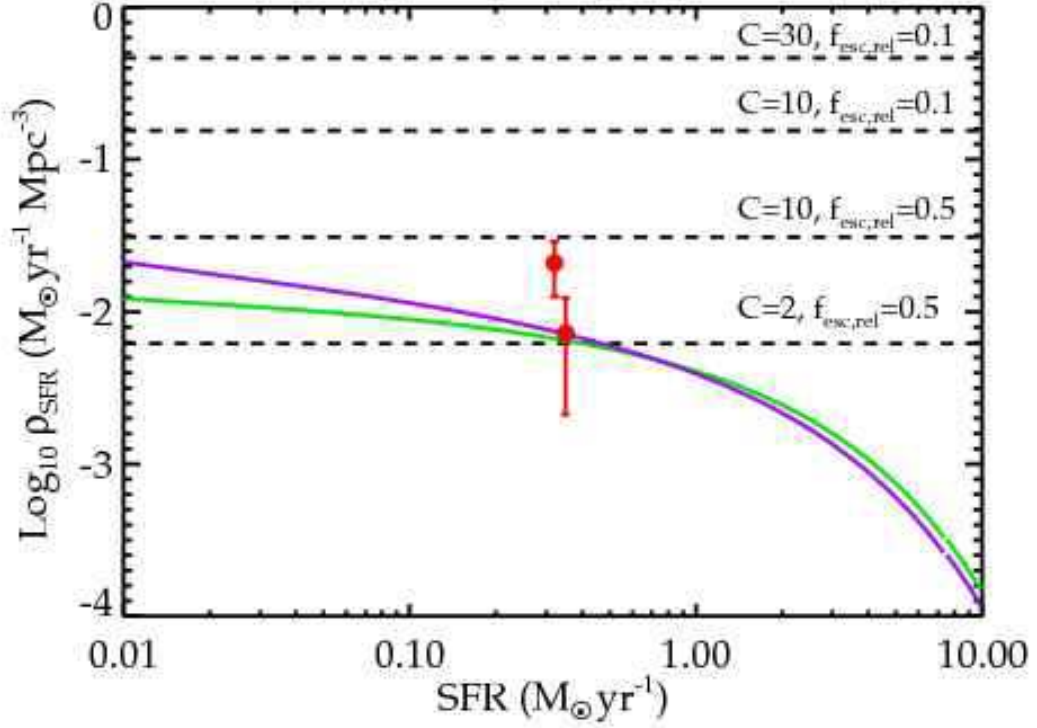


Fig. 16.— The cumulative comoving density of star formation rate at $z \simeq 7.5$ derived for the two extreme (two last entries of Table 8) luminosity functions from Bouwens et al. (2008) with faint end slopes of $\alpha = 2.0$ (purple) or $\alpha = 1.4$ (green). Two constraints from the present survey are shown as red points. The upper point assumes 6 sources are at high redshift; the lower point assumes only the two most promising candidates. The density necessary to keep the IGM reionized at $z = 7.5$, calculated from Eq. 1 for a range of clumping factors C and escape fraction $f_{esc,rel}$, is shown as the dashed lines.